Supplement for "Ground-based MAX-DOAS observations of tropospheric aerosols, NO_2, SO_2 and HCHO in Wuxi, China, from 2011 to 2014"

Y. Wang[1], J. Lampel[1,2], P. H. Xie[3,4,5], S. Beirle[1], A. Li[3], D. X Wu[3], and T. Wagner[1]

[1] Max Planck Institute for Chemistry, Mainz, 55128, Germany
[2] Institute of Environmental Physics, University of Heidelberg, Heidelberg, 69120, Germany
[3] Anhui Institute of Optics and Fine Mechanics, Key laboratory of Environmental Optics and Technology, Chinese Academy of Sciences, Hefei, 230031, China
[4] CAS Center for Excellence in Urban Atmospheric Environment, Institute of Urban Environment, Chinese Academy of Sciences, Xiamen, 361021, China
[5] School of Environmental Science and Optoeclectronic Technology, University of Science and Technology of China, Hefei, 230026, China

Correspondence to: Y. Wang (y.wang@mpic.de); P.H. Xie (phxie@aiofm.ac.cn)

1 DOAS analysis and data screening

In the DOAS analysis, the slant column densities (SCDs) of the trace gases (TGs) are retrieved from the off-axis spectra using a zenith measurement from the same elevation sequence as the Fraunhofer reference spectrum (FRS). As the latter also contains (usually small) absorptions features, the resulting SCD actually represents the differences between the SCDs of the measured spectrum and the FRS. This difference is usually referred to as the differential SCD (dSCD). The use of a FRS from the same elevation sequence can minimise any effects caused by changes of the properties of the instrument (relevant for long term analyses) and the stratospheric absorptions (relevant for measurements at high solar zenith angle (SZA)). The effect of rotational Raman scattering is considered by including a Ring spectrum (Shefov 1959; Grainger and Ring, 1962; Chance and Spurr, 1997; Solomon et al., 1987; Wagner et al., 2009) computed by the DOASIS software (Kraus, 2006, using a routine from Bussemer 1993). To account for the different wavelength dependencies of the filling-in in clear and cloudy skies, an additional Ring spectrum as described in Wagner et al. (2009) is also included.

For the retrieval of O_4 and NO_2, the wavelength range of 351 to 390 nm is selected, covering two O_4 absorption bands and several NO_2 absorption bands. A 3rd order polynomial is used. Besides the NO_2 cross section at the temperature of 294 K, another cross section at 220 K is also included in the fit to account for the temperature dependence of the NO_2 absorptions. The detailed DOAS settings for the retrieval are listed in Table 1 of the main manuscript. In Fig. S1a and b, the O_4 and NO_2 dSCDs from all measurements are plotted against SZA. NO_2 and O_4 dSCDs show an obvious systematic increase or decrease, respectively, for SZA larger than 75 °. For NO_2 this behaviour can be explained by the larger differences of the stratospheric light paths between the measurement and the FRS for large SZA. The opposite dependencies in the morning and evening

(indicated by the different solar azimuth angles) are due to the decrease or increase of the stratospheric light path with time in the morning and evening, respectively. The O_4 behaviour might be related to the interference of the so called intensity offset (see below) and the O_4 absorption. But this hypothesis is still not clearly confirmed.

A quite large relative intensity offset (RIO) is found for measurements at large SZAs as indicated in Fig. S1c, which implies a possible interference of the offset corrections and the derived TG dSCDs (see also Coburn et al., 2011). Thus we skip the data for the SZA larger than 75° to avoid the interference with the stratospheric contributions and RIO on the retrieved tropospheric dSCDs.

SO_2 dSCDs are retrieved in the wavelength interval from 307.8 nm to 330 nm including O_3, SO_2, HCHO cross sections and Ring spectra shown in Table 1 of the main manuscript. Wang et. al (2014) performed sensitivity studies to find the optimum wavelength interval which minimizes both random and systematic uncertainties on the SO_2 retrieval. They found that the wavelength range of 305 to 317.8 nm provides the lowest fitting errors. Below 305 nm, interference with the strong ozone absorption can affect the SO_2 retrieval. At small wavelengths also the signal to noise ratio decreases. Considering the rather low sensitivity of the miniature spectrometer in the UV range used in our study compared to scientific grade spectrometer used in the study of Wang et. al (2014), here we limit the lower wavelength range to 307.8 nm. We also changed the upper wavelength range to 330 nm to minimise the possible interference with other species. The SO_2, O_3 and Ring dSCDs as well as the intensity offset are plotted against SZAs in Fig. S2. At large SZAs strong changes of all quantities are found indicating the possible interference of the stratospheric ozone absorptions and the intensity offset on the SO_2 retrieval. To avoid these interferences, we screen the SO_2 dSCD data for SZA larger than 75°.

HCHO dSCDs are retrieved in the wavelength interval from 324.6 to 359 nm including O_3, O_4, SO_2, HCHO cross sections and Ring spectra shown in Table 1 of the main manuscript. Pinardi et. al (2013) found that the interferences between BrO, Ring spectrum and HCHO can strongly affect the retrieved HCHO dSCDs and they recommended the wavelength range of 336.5 to 359 nm, to minimise the uncertainties of the HCHO retrieval. In the wavelength range below 336.5 nm, the ozone absorption interferes with the HCHO retrieval, like for SO_2. However this conclusion is only appropriate for the retrieval with the daily noon zenith spectrum as the FRS. In this study, the sequential FRS is used. Because BrO is mostly located in the stratosphere, the difference of the BrO absorptions between the measurement and the FRS is negligible (the differential optical depth of the BrO absorption is typical only 1×10^{-4}) and much lower than using a daily noon FRS (typical 6×10^{-4}). Considering that the BrO absorption signal is too weak to impact the HCHO retrieval, the BrO cross section is not included in the HCHO DOAS fit in this study. Tropospheric BrO is not expected to be found due to large NO_2 concentrations (e.g. Holla et al 2015). Moreover similar to the BrO interference, the effective stratospheric ozone absorption is also much smaller if a sequential FRS is used compared to a daily noon FRS. Thus the wavelength interval can be extended to a shorter wavelength to cover more and stronger absorption bands of HCHO. Moreover a wider wavelength range usually makes the fit more stable, but at shorter wavelengths the interference of the ozone absorption is also stronger. To find the optimal retrieval wavelength interval, the examples of the HCHO retrieval in three different wavelength ranges of 310 to 359 nm, 324.6 to 359 nm and 336.5 to 359 nm are shown in Fig. S3. The measured structure from the DOAS fit in the wavelength

range 310 to 359 nm indicates the strong interference of the ozone absorption. In addition, the HCHO dSCDs and the fitting errors in the three wavelength ranges on two days with low and high HCHO load are shown in Fig. S4. We find that the HCHO dSCDs in the wavelength range of 324.6 to 359 nm are consistent with those in 336.5 to 359 nm, which is recommended by Pinardi, et. al (2013). And both of them are quite different from the values in the wavelength range of 310 to 359 nm, especially on the day with the low HCHO load. The reverse "U" diurnal variation of the HCHO dSCDs in the wavelength range of 310 to 359 nm is an indication for the strong interference of the stratospheric ozone absorption. Moreover the wavelength range of 324.6 to 359 nm has much smaller fitting errors than the wavelength range of 336.5 to 359 nm. Thus we conclude that in general the wavelength range of 324.6 to 359 nm is the optimal wavelength range in which the ozone interference is weak and the fitting error is small. To avoid remaining interferences of the HCHO results with the stratospheric ozone absorption and intensity offset we exclude the HCHO dSCD for SZA > 75 °(see. Fig. S5).

After applying these filters, the mean RMS of the residual is 6×10^{-4} for NO_2, O_4 and HCHO, and 1.3×10^{-3} for SO_2. The detection limit of the dSCDs (assumed to as two times of the mean RMS) is 3×10^{15} molecules cm^{-2} for NO_2, 5×10^{41} molecules^2 cm^{-5} for O_4, 5×10^{15} molecules cm^{-2} for SO_2, 5×10^{15} molecules cm^{-2} for HCHO. Only 0.7%, 0.4%, 3.3%, 6.6% of the filtered measurements have results below the respective detection limits for NO_2, O_4, SO_2 and HCHO, respectively.

2 PriAM inversion algorithm

The profile inversion is based on the fact that the vertical distribution of the light paths depends on the elevation angle of the observation. The vertical trace gas profiles are assumed to be constant for the duration of the elevation angle sequence and also in horizontal dimensions. If the light paths are well-known, vertical trace gas profiles can be derived from a set of dSCDs for the different elevation angles. Besides the observation geometry and sun position, scattering on air molecules (Rayleigh scattering), aerosols and cloud particles (often referred to as Mie scattering) determine the atmospheric light paths. Opposed to the well-known Rayleigh scattering, scattering on aerosols and cloud particles depends on their respective optical properties, which are diverse and depend on a size, shape and composition. Vertical profiles of AEs can be retrieved from a set of O_4 dSCDs for individual elevation sequences using the well-known vertical profile of the O_4 concentration, which is proportional to the square of the concentration of molecular oxygen and thus only depends on temperature and pressure (Hönninger et al., 2004; Wagner et al., 2004; Frieß et al., 2006). Like for other algorithms, a two step inversion procedure is also used in the PriAM algorithm: in the first step the aerosol extinction (AE) profiles and in the second step the profiles of the trace gas VMRs are retrieved. In PriAM we applied the Levenberg-Marquardt modified Gauss-Newton procedure (Rodgers, 2000) to solve the ill-posed inversion problem for AEs (Frieß, et al., 2006 and Yilmaz, 2012) through the numerical iteration:

$$x_{i+1} = x_i + \left((1+\gamma_i)S_a^{-1} + K_i^T S_\varepsilon^{-1} K_i\right)^{-1} (K_i^T S_\varepsilon^{-1}(y - F(x_i)) - S_a^{-1}(x_i - x_a)) \quad \text{(s1)}$$

with x_{i+1} and x_i the solutions of atmospheric state at the i and i+1 step. x_a is the a-priori profile and y the measurement vector. γ_i is the Levenberg-Marquardt factor, which is multiplied or divided by two to make the minimization of the cost function faster and more stable than for the normal Gauss-Newton algorithm. S_a is the covariance of the error of the a-priori profile and S_ε is the covariance of the errors of the measurements. K_i and $F(x_i)$, which are calculated for each iteration step, are the weighting function and the forward model value at the state of x_i, respectively.

The set of O_4 dSCDs for the m non-zenith elevation angles in each scan (in this study 5°, 10°, 20°and 30°) is the measurement vector to retrieve the AE (σ) in n atmospheric layers. In this study 20 atmospheric layers from the surface to 4 km with height intervals of 0.2 km are used (the same layers are used for the retrievals of the trace gas profiles). Considering the frequent variation of aerosols, very little is known about the expected AE profile. Thus a fixed smoothed box-shaped a-priori AE profile (Boltzmann distribution) is used, as introduced by Yilmaz (2012):

$$\sigma(z) = \frac{\sigma(0)}{1+\exp\left(\frac{z-\frac{\tau}{\sigma(0)}}{0.3}\right)} \quad \text{(s2)}$$

Here σ(z) and σ(0) denote the extinction coefficient at the altitude z (km) and at the surface, respectively. τ is the optical depth. In this study, σ(0) and τ are 0.15 km^{-1} and 0.3, respectively. The covariance matrix S_a is constructed as follows:

$$S_{a\,ik} = \sigma_{a_i}^2 \times e^{-\frac{|z_i - z_k|}{\eta}} \quad \text{(s3)}$$

With σ_{a_i} the a-priori AE at the atmospheric layer i. z_i and z_k are the heights of the atmospheric layer i and k, respectively. The smoothing factor η is 0.5 km. The covariance matrix of the measurement uncertainties S_ε contains diagonal elements representing the square of the fitting errors of the O_4 dSCDs and off-diagonal elements of zero.

In most previous studies, the optimal linear inverse method (Rodgers, 2000; Frieß, 2011) is used to retrieve the vertical profiles of the trace gas VMRs. In PriAM, we use the Gauss-Newton numerical procedure as in eq. (s1) because the use of the safe state of AEs and trace gas VMRs (see below) converts the linear problem into a nonlinear one.

Similar to the retrieval of the AE profiles, the diagonal element of S_ε is the square of the fitting errors of the respective trace gas dSCDs and the off-diagonal elements are zero. The elements of S_a are calculated from eq. s3 but the σ_{a_i} are replaced by the a-priori VMR of the respective trace gas (ρ_{a_i}). One fixed a-priori profile of the VMRs for each trace gas is used. The a-priori profiles of NO_2 and SO_2 are described as an exponential function (similar to Yilmaz, 2012 and Hendrick et al 2014):

$$\rho(z) = \rho(0) \times e^{-\frac{z}{H}} \quad \text{(s4)}$$

Here ρ(z) and ρ(0) are the VMR of the trace gases at altitude z (km) and near the surface, respectively. H is the scaling height (in this study fixed to 1km). The ground VMR ρ(0) is set to 4 ppb for NO_2 and 8 ppb for SO_2.

MAX-DOAS and aircraft measurements in Milano during summer of 2003 indicated that the layer of high HCHO concentration often extends to 1 km or even higher altitudes (Wagner et al., 2011, Junkermann, 2009). Thus for HCHO the same a-priori profile (Boltzmann distribution) as for the AE is used. The surface mixing ratio ρ(0) is set to 4ppb and the VCD to 1.7×10^{16} molecules/cm^2.

During the profile inversion for aerosols and trace gases, negative values can occur, which are physically invalid. To avoid them, the original atmospheric state vector x is transformed to its corresponding 'safe state' x' (Yilmaz, 2012):

$$x' = \ln(x) \tag{s5}$$

After finishing the calculation of x', x' is transformed back to the original format

$$x = e^{x'} \tag{s6}$$

In this way it is ensured that x is always positive.

The averaging kernel (AK) is an important quantity to characterize the vertical resolution of the measurement and the sensitivity of the retrieved state $\hat{x}$ to the true state as a function of altitude. The trace of the averaging kernel matrix yields the degree of freedom (DoF) of the signal, which represents the number of independent pieces of information that can be retrieved. The error of the retrieved state S consists of the smoothing error S_s (due to the limited vertical resolution of the retrieval) and the retrieval noise S_m (due to measurement errors).

2.1 Influence of the choice of the a-priori profiles on the retrieved profiles

We investigate the impact of the choice of the a-priori profiles on the retrieved profiles, VCD (AOD) and near-surface VMR (AE) (from the ground to 200 meters) for two months (July 2011 and February 2012) by either varying the VCD (AOD) by 0.5 or 2, or changing the profile shape by replacing the Boltzmann distribution with the exponential distribution (for aerosols and HCHO) or the other way around (for NO_2 and SO_2) (see Fig. S6 in the supplement). We compared the respective differences of the measured dSCDs and modeled dSCDs (results of the forward model) and the retrieved profiles (see Fig. S7), VCDs (AODs) and the near-surface VMRs (AEs) (see Table S1). We found a stronger influence of the a-priori profile for aerosols than for the trace gases. By changing the a-priori profiles, the maximum change of the retrieved VCDs and AODs is on average about 10% and 20%, respectively. The retrieved near-surface VMRs and AEs change by around 2% and 10%, respectively. For both aerosols and trace gases, typically the smallest differences between the measured and modeled dSCDs are found for the standard a-priori profiles (see Fig. S7) indicating that the standard a-priori profiles are the preferred assumptions.

3 Deriving O_4 VCDs from the measured surface temperature and pressure

To derive O_4 VCDs from the measured surface temperature and pressure (TP), we first fit 6th order polynomials to the seasonal variations of surface TP (see Fig. 3 in the main manuscript). Second, we calculate height profiles of the temperature assuming a lapse rate of 0.645K / 100m:

$$T_{i+1} = \begin{cases} T_i - 0.645 \times \frac{z_{i+1} - z_i}{0.1} & (0 < z < 12km) \\ T(z = 12km) & (z > 12km) \end{cases} \tag{s7}$$

Here T_i (in unit of kelvin, K) and z_i indicate the temperature and height of the atmospheric layer i, respectively. Above 12 km the temperature is kept constant to represent the temperature inversion around the tropopause. Here it should be noted that this simplification has only negligible influence on the derived O_4 VCD, because most of the O_4 is present at lower altitudes. For the same reason, the TP profiles are only calculated up to an altitude of 20 km.

Based on the calculated temperature profile and the surface pressure we calculate the corresponding pressure profile:

$$D_i = 28.9 \times 10^{-3} \times {}^{P_i}/_{(T_i \times R)} \quad \text{(s8)}$$

$$P_{i+1} = P_i - (g \times 100 \times D_i) \quad \text{(s9)}$$

Here D (in units of kg/m^3) and P (in unit of hPa) indicate the air density and pressure, respectively. R is the ideal gas constant (8.31 J/mol K), and g is the gravitational constant (9.8 N/kg). Because the O_4 concentration is proportional to the square of the oxygen concentration (which represents 21% of the air density), the profile and VCD of O_4 can be calculated from the assumed air density profile. Fig. 3 in the main manuscript shows the seasonal variation of the O_4 VCD calculated from the measured surface TP in 2012. The O_4 VCD in summer is systematically lower than in winter (by about 2×10^{42} molecules^2 cm^{-5}, which is about 15% of the annually mean O_4 VCD).

4 Dependencies of the errors of the VCD derived by the geometric approximation and the profile inversion on the aerosol load

In Fig S9, $Diff_{total}$, $Diff_{\text{inversion}}$ and $Diff_{geometry}$ for the different TGs are plotted against the for elevation angles of 20° and 30° (for a range of the RAA between 100° to 110. We found linear relations of $Diff_{geometry}$ against AOD for the three species, especially for 20° elevation angle. The weaker dependence of $Diff_{geometry}$ on AODs for an elevation angle of 30° is due to the lower sensitivity of MAX-DOAS observations on aerosols than for an elevation angle of 20°. Correlation coefficients of the linear regressions of $Diff_{geometry}$ and AODs are largest for HCHO due to its higher layer height compared to the other species. The same reason causes the better correlation for SO_2 than for NO_2. For relatively large AODs, the relation of $Diff_{total}$ and AOD follows a linear relation of $Diff_{geometry}$ and AODs, but for low AODs, $Diff_{\text{inversion}}$ contributes most to $Diff_{total}$. $Diff_{\text{inversion}}$ is mostly between ±20% and is randomly distributed around zero. Thus $Diff_{\text{inversion}}$ can not be the reason for the systematic bias between the VCD_{geo} and the VCD_{pro}.

Figures

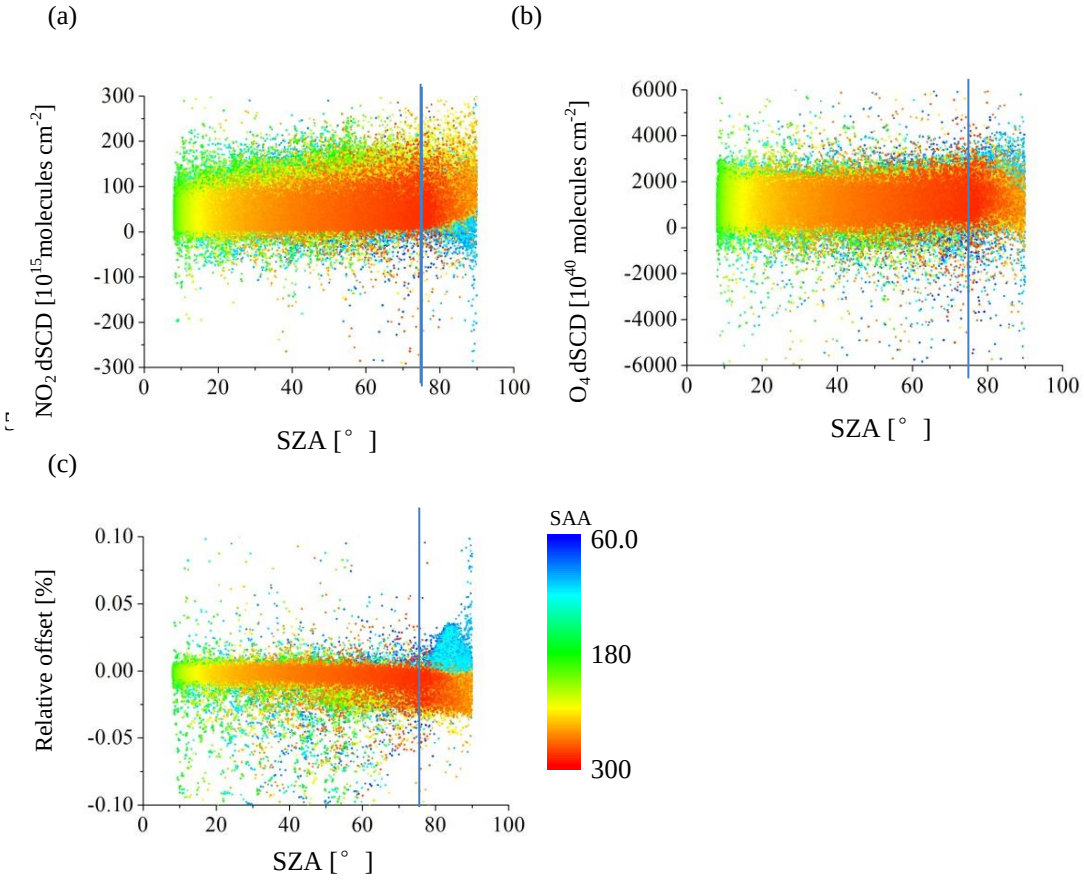

Figure S1: SZA dependence of the NO_2 dSCDs (a), O_4 dSCDs (b) and relative intensity offset (c) derived from the NO_2 DOAS fits for all measured spectra during the whole observation period. The blue vertical lines indicate a SZA of 75 °. The colours indicate the solar azimuth angle (SAA) with north as zero. Small (large) RAA indicate measurements in the morning (evening).

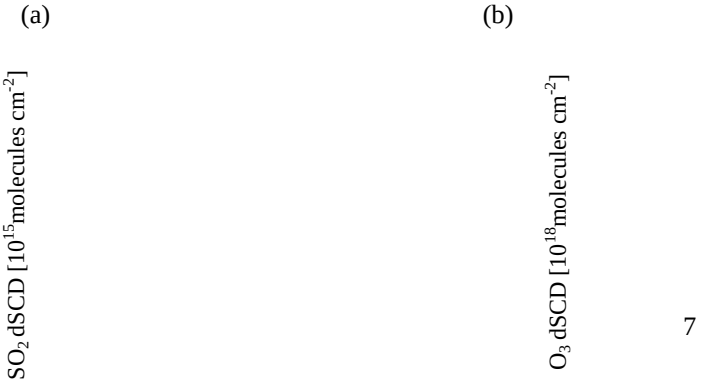

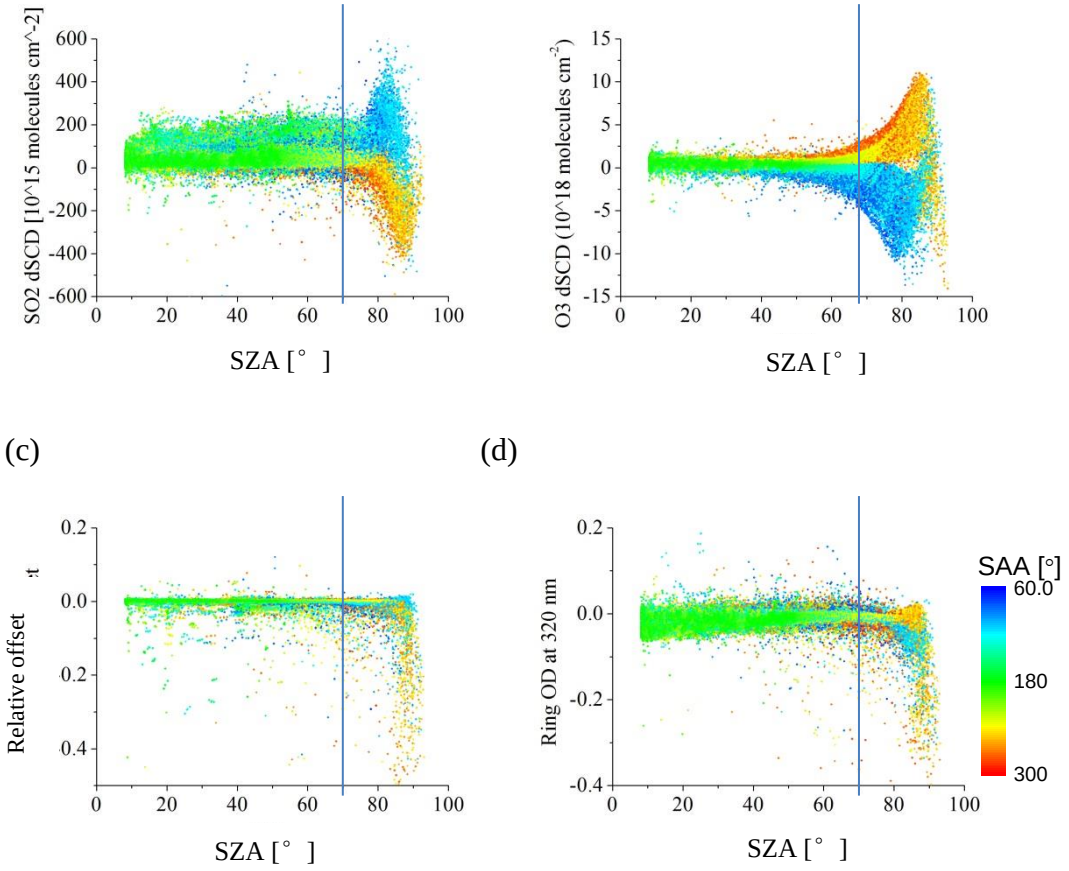

Figure S2: SZA dependence of the SO_2 dSCDs (a), O_3 dSCDs (b), relative intensity offset (c) and Ring optical depth (d) derived from the SO_2 DOAS fits for all measured spectra during the whole observation period. The blue lines indicate a SZA of 75 °. The colours indicate the solar azimuth angle (SAA) with north as zero. Small (large) RAA indicate measurements in the morning (evening).

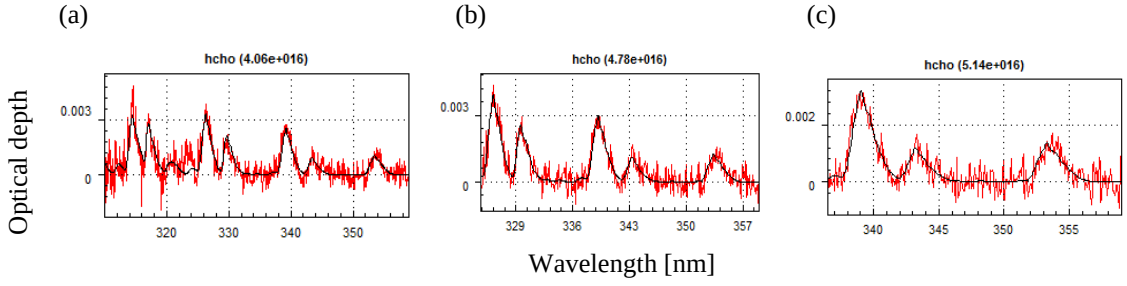

Figure S3: Examples of DOAS fits of HCHO in the wavelength ranges of 310 to 359 nm (a), 324.6 to 359 nm (b) and 336.5 to 359 nm (c). The black curve and red curve are the fitted and measured HCHO absorption structures, respectively.

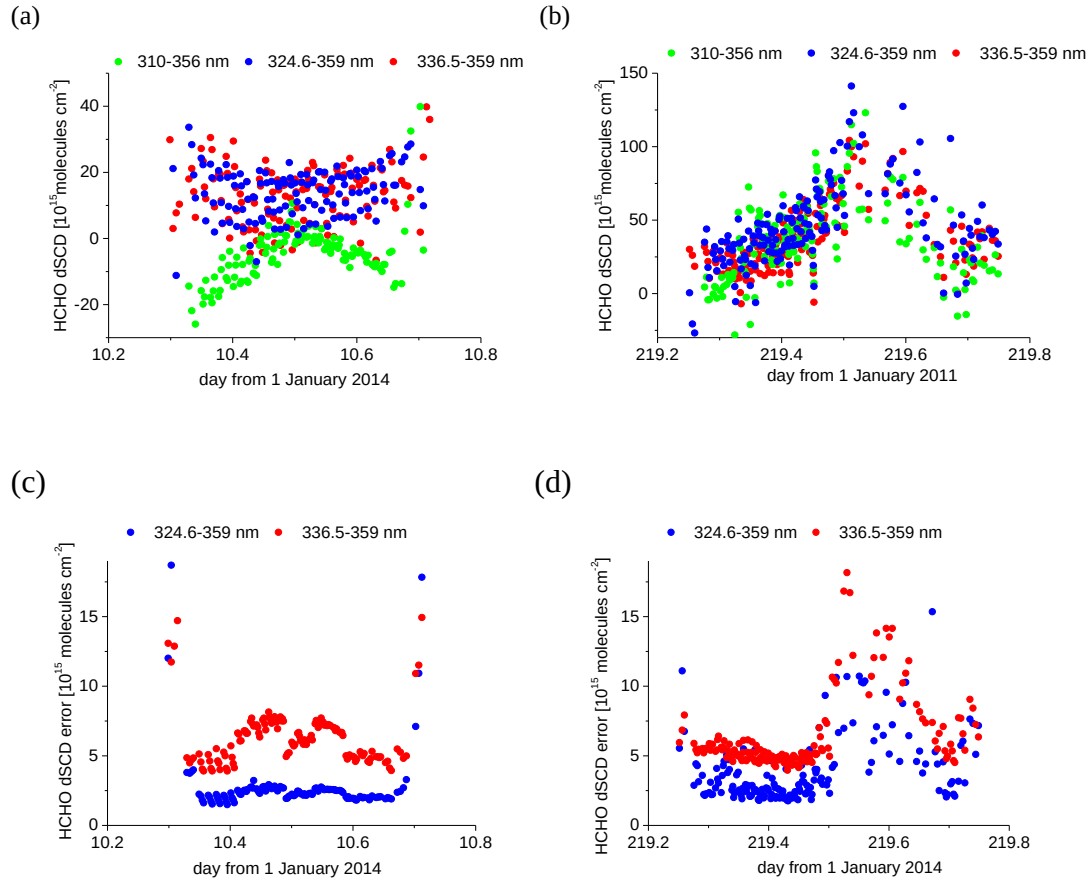

Figure S4: HCHO dSCDs derived from the DOAS fits in the three wavelength ranges on 10 January (a) and 7 August 2014 (b) as well as the fit errors in the wavelength ranges of 324.6-359 nm and 336.5-359 nm on the both days in (c) and (d).

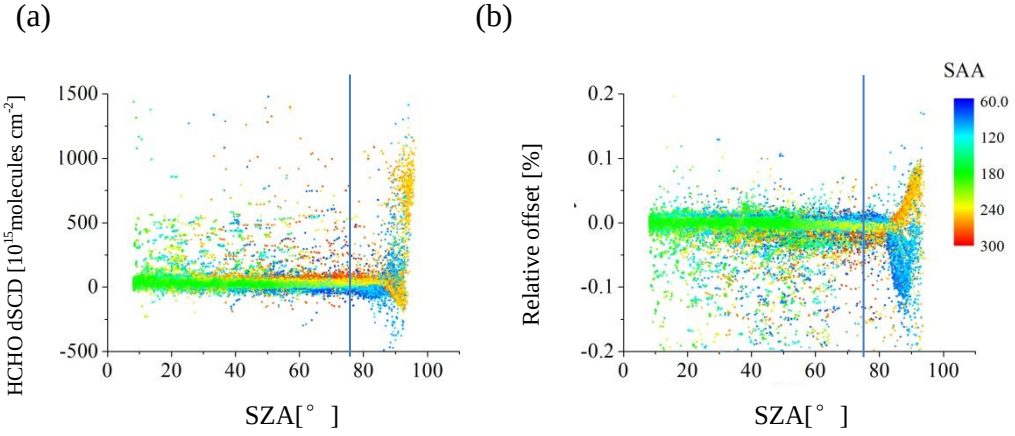

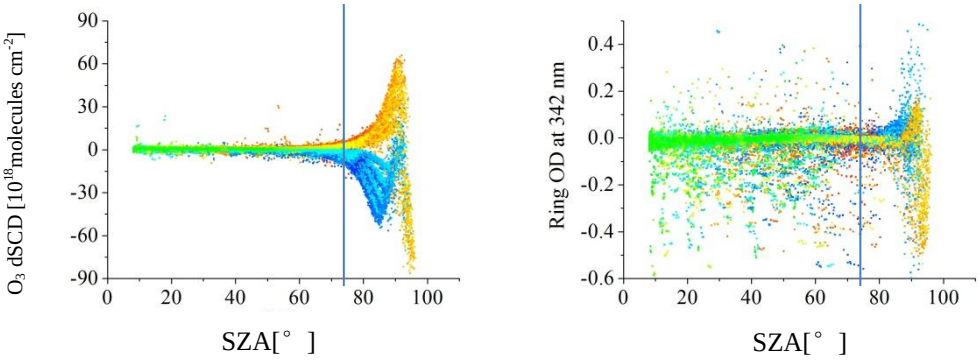

Figure S5: SZA dependence of the HCHO dSCDs (a), relative intensity offset (b), O_3 dSCDs (c), and Ring optical depths (d) derived from the HCHO DOAS fits of all measured spectra during the whole observation period. The blue lines flag the position of SZA of 75 °. The blue lines indicate a SZA of 75 °. The colours indicate the solar azimuth angle (SAA) with north as zero. Small (large) RAA indicate measurements in the morning (evening).

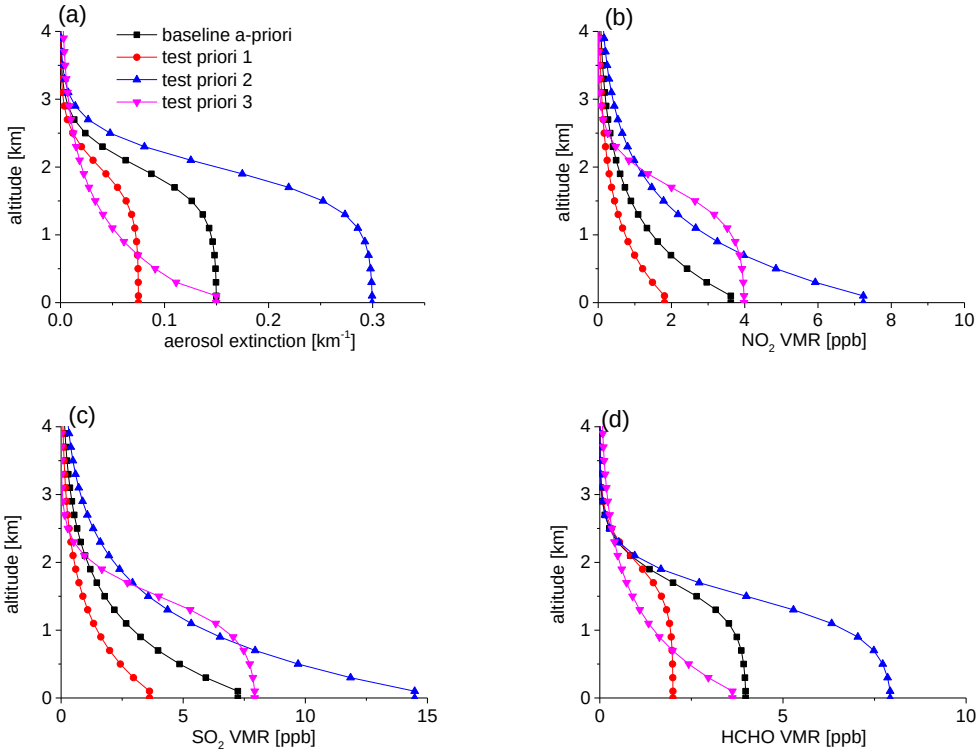

Figure S6: Four a-priori profiles for aerosol extinction (a), NO_2 VMRs (b), SO_2 VMRs (c) and HCHO VMRs (d) used for the sensitivity tests of the MAX-DOAS profile retrievals. The baseline a-priori profile is used for the standard retrieval of the whole measurements.

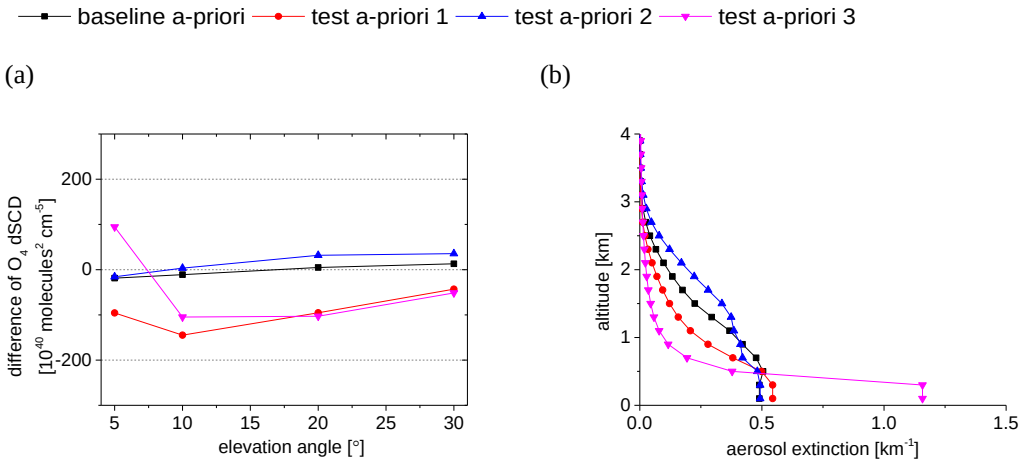
baseline a-priori
test a-priori 1
test a-priori 2
test a-priori 3
(a)
(b)
difference of O4 dSCD [10^40 molecules^2 cm^-5]
elevation angle [°]
altitude [km]
aerosol extinction [km^-1]
(c)
(d)
difference of NO2 dSCD [10^15 molecules cm^-2]
elevation angle [°]
altitude [km]
NO2 VMR [ppb]
(e)
(f)
difference of SO2 dSCD [10^15 molecules cm^-2]
elevation angle [°]
altitude [km]
SO2 VMR [ppb]
(g)
(h)

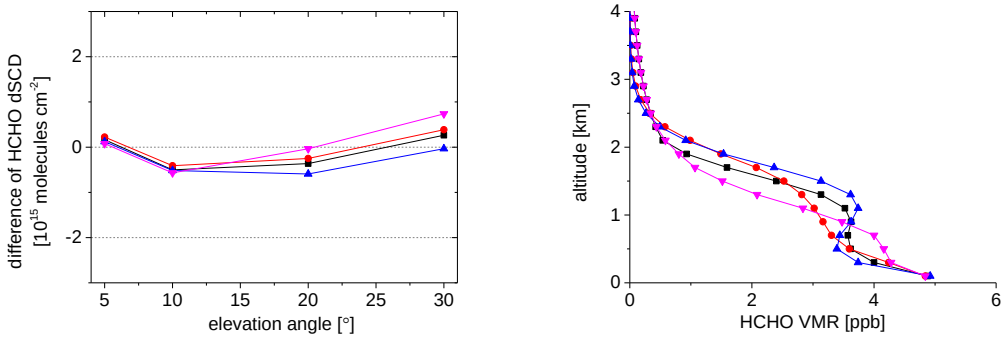

Figure S7: Left: Elevation angle dependencies of the differences between measured and modelled dSCDs of O_4, NO_2, SO_2 and HCHO for the different a-priori profiles shown in Fig. S6. Right: the average profiles of AE, NO_2 VMR, SO_2 VMR and HCHO VMR derived for the different a-priori profiles. The results are obtained for measurements in July 2011 and February 2012.

5

(a) (b)

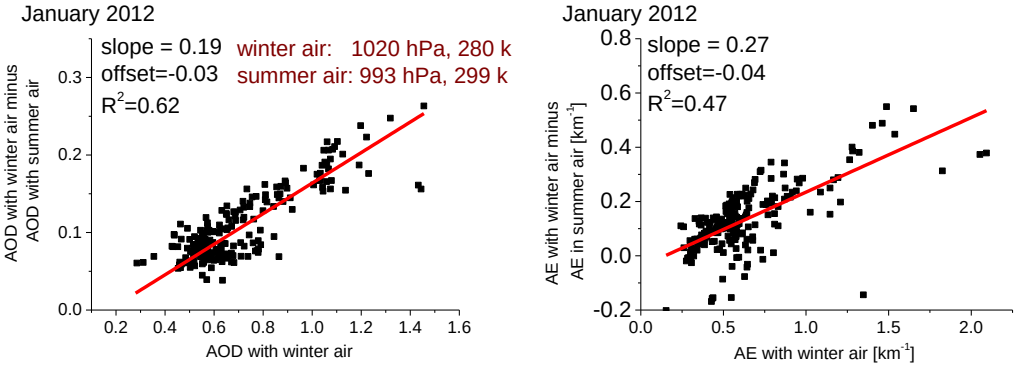

10

Figure S8: Dependence of the difference of the AOD (left) and AE (right) for January 2011 retrieved using TP profiles for either winter or summer versus the AOD and AE (retrieved using TP profiles for winter). TP profiles for winter are calculated assuming a surface pressure of 1020 hPa and surface temperature of 280 K; those for summer are calculated assuming a surface pressure of 993 hPa and surface temperature of 299 K. The retrievals based on the wrong (summer) TP profiles underestimate the AODs and
15 **near-surface AEs by about 20% and 27%, respectively.**

(a)

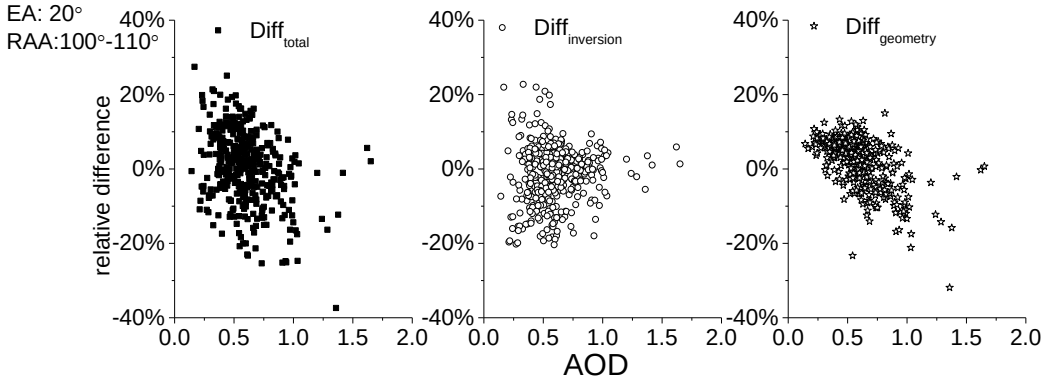
EA: 20°
RAA:100°-110°
Diff total
Diff inversion
Diff geometry
relative difference
AOD

(b)

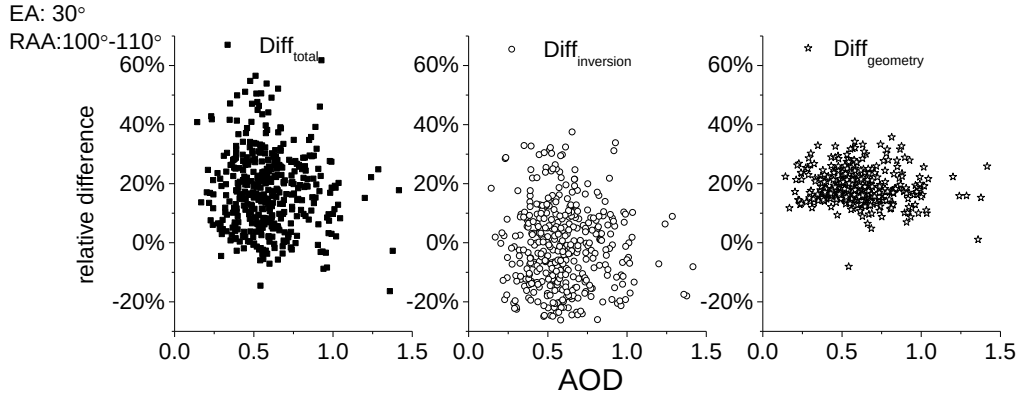
EA: 30°
RAA:100°-110°
Diff total
Diff inversion
Diff geometry
relative difference
AOD

(c)

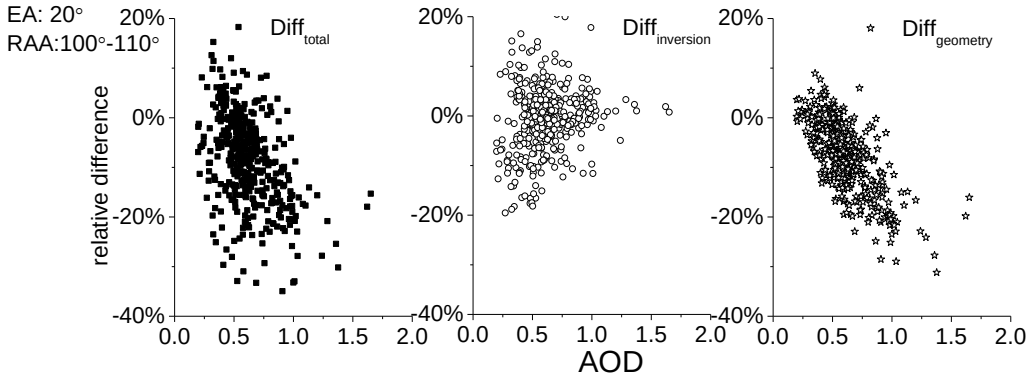
EA: 20°
RAA:100°-110°
Diff total
Diff inversion
Diff geometry
relative difference
AOD

(d)

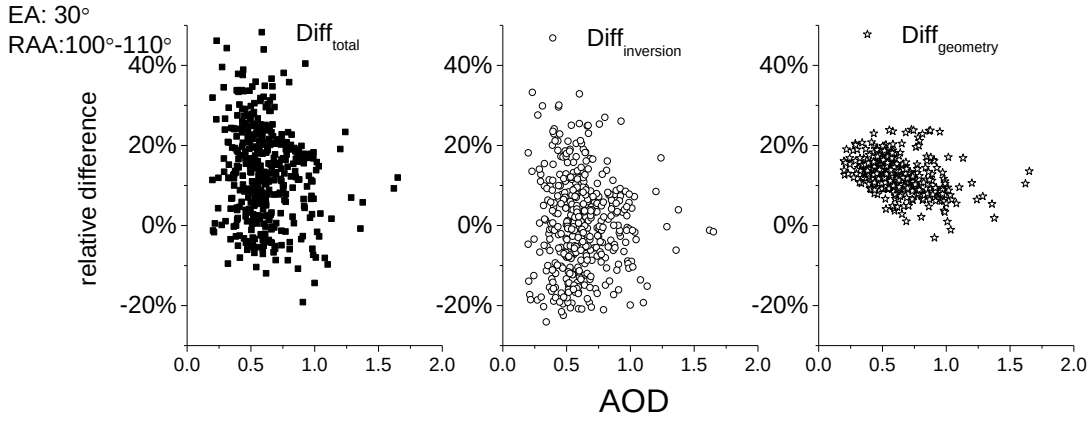

(e)

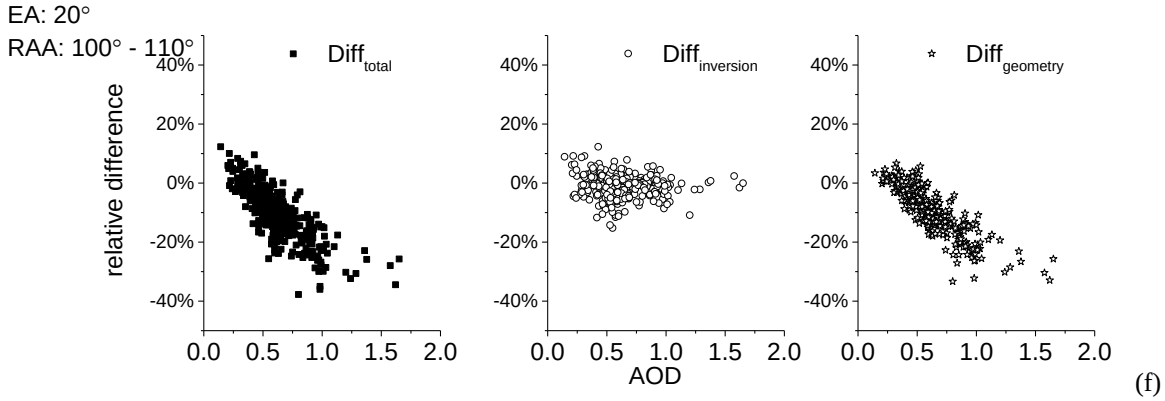

(f)

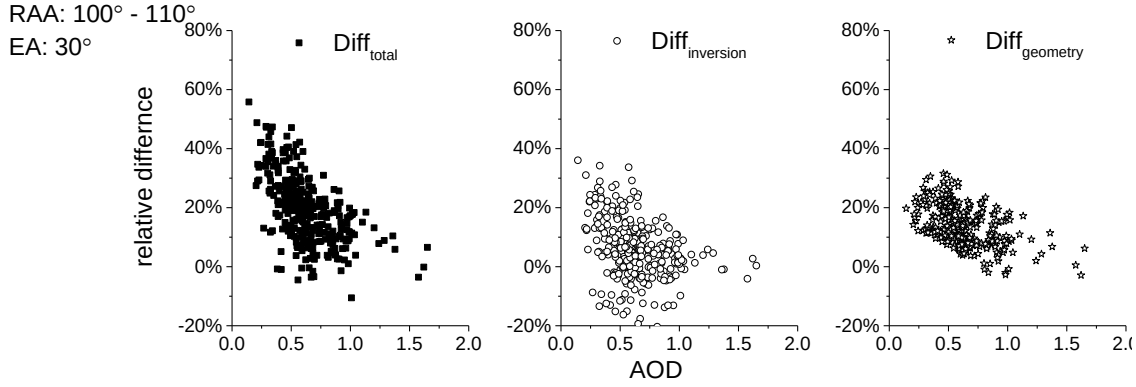

Figure S9: $Diff_{total}$, $Diff_{\text{inversion}}$ and $Diff_{geometry}$ derived for MAX-DOAS observations under clear sky conditions at RAA between 100 ° and 110 ° for NO_2 (a), SO_2 (c), HCHO (e) for elevation angle of 20 °; the corresponding results for an elevation angle of 30 ° are shown in sub-figures (b), (d), (f).

pressure temperature

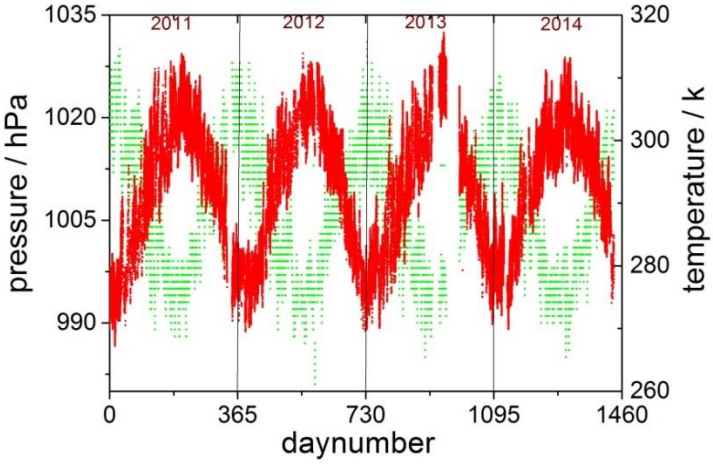

Figure S10: Time series of near-surface temperature and pressure obtained from the ground-based weather station near the MAX-DOAS instrument from 2011 to 2014.

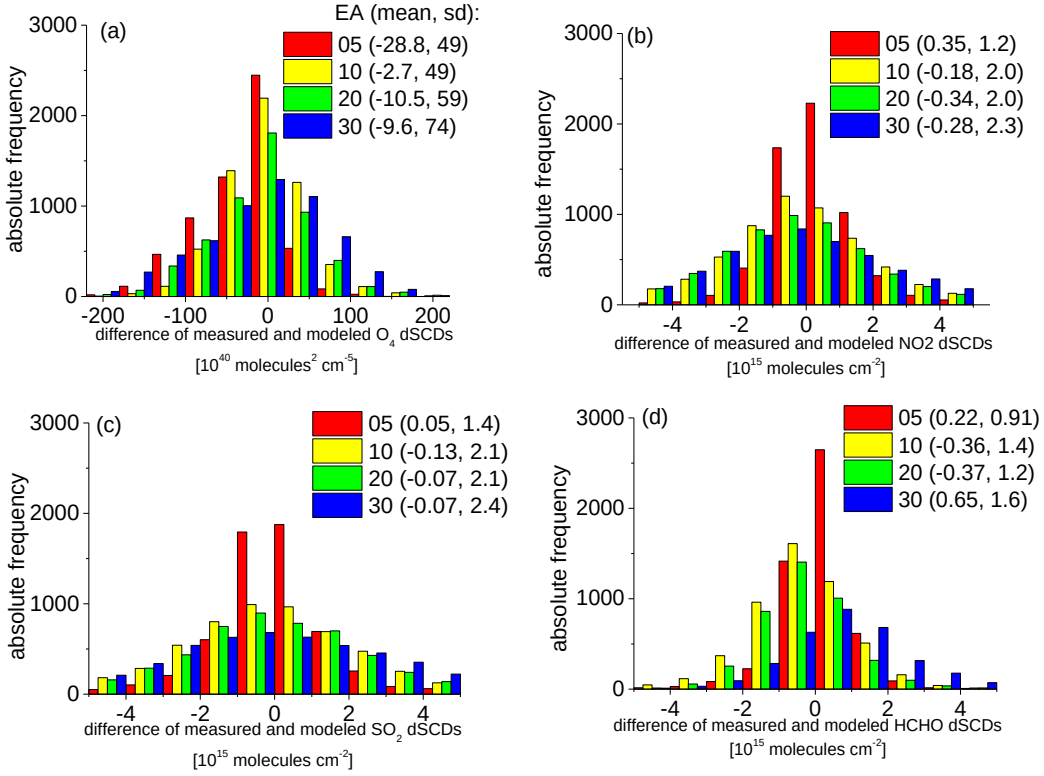

Figure S11: Frequency distributions of the differences between measured and modelled dSCDs for observations at clear sky with low aerosols: O_4 (a), NO_2 (b), SO_2 (c) and HCHO (d). The different elevation angles are indicated by the different colors. The mean values and standard deviations are given in brackets.

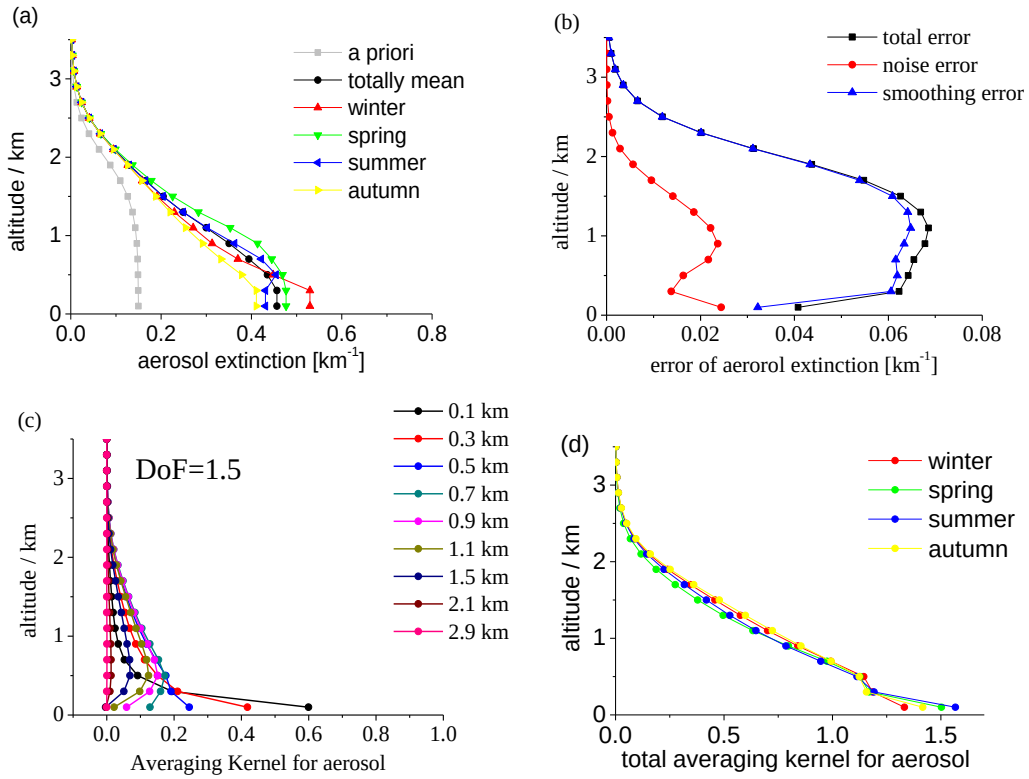

Figure S12: (a) Mean AE profiles for the different seasons derived from observations under clear sky conditions with low aerosols. Also shown is the a-priori profile; (b) total, noise and smoothing errors of the averaged aerosol extinction profile; (c) the corresponding mean averaging kernels for the different height layers (DoF is the degree of freedom); (d) the total averaging kernel for the different seasons.

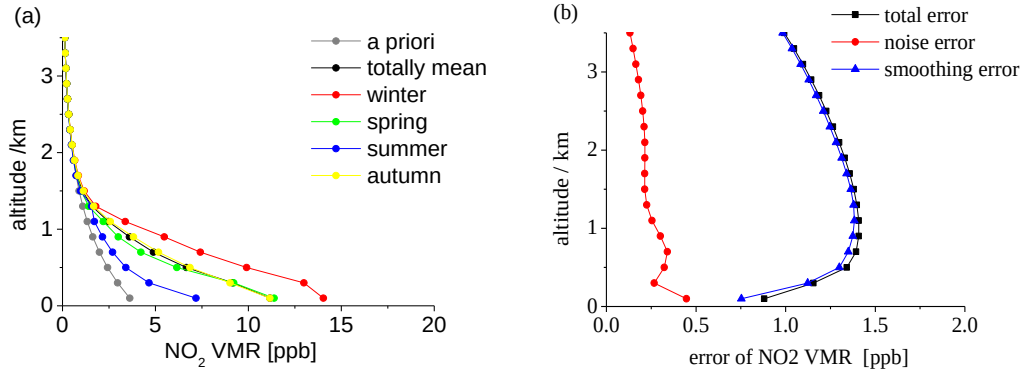

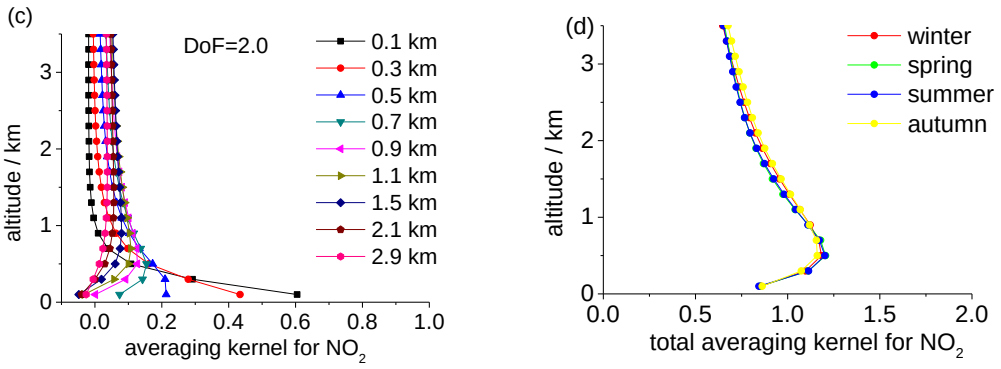

Figure S13: Same as Fig. S12, but for the NO_2 retrieval.

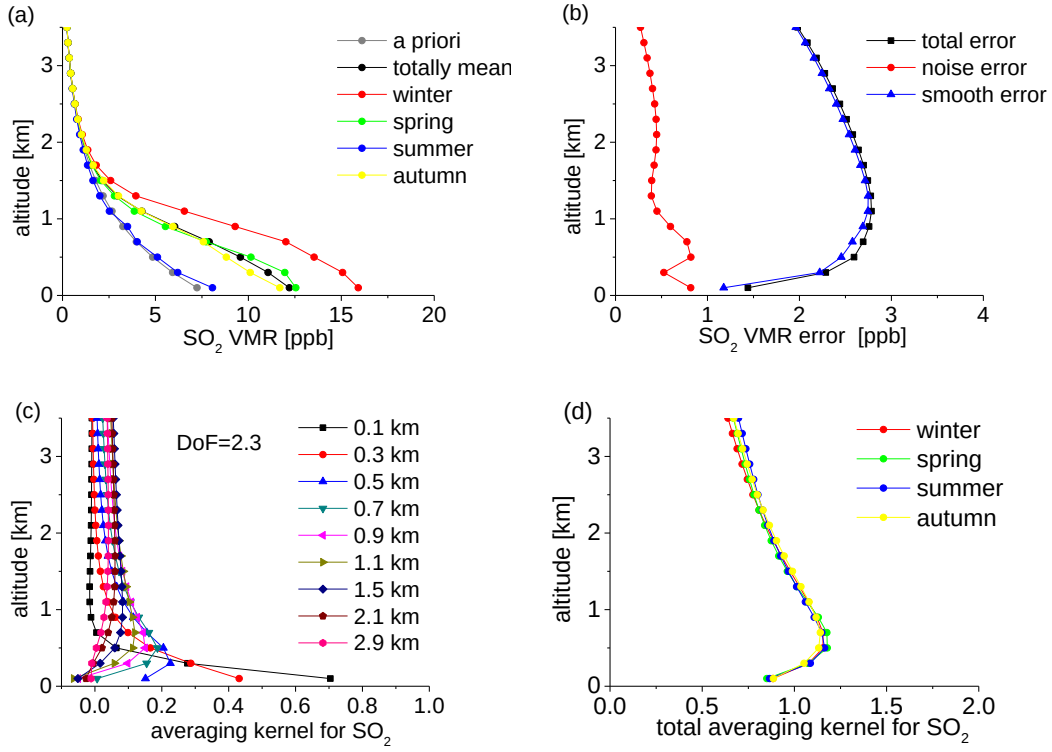

Figure S14: Same as Fig. S12, but for the SO_2 retrieval.

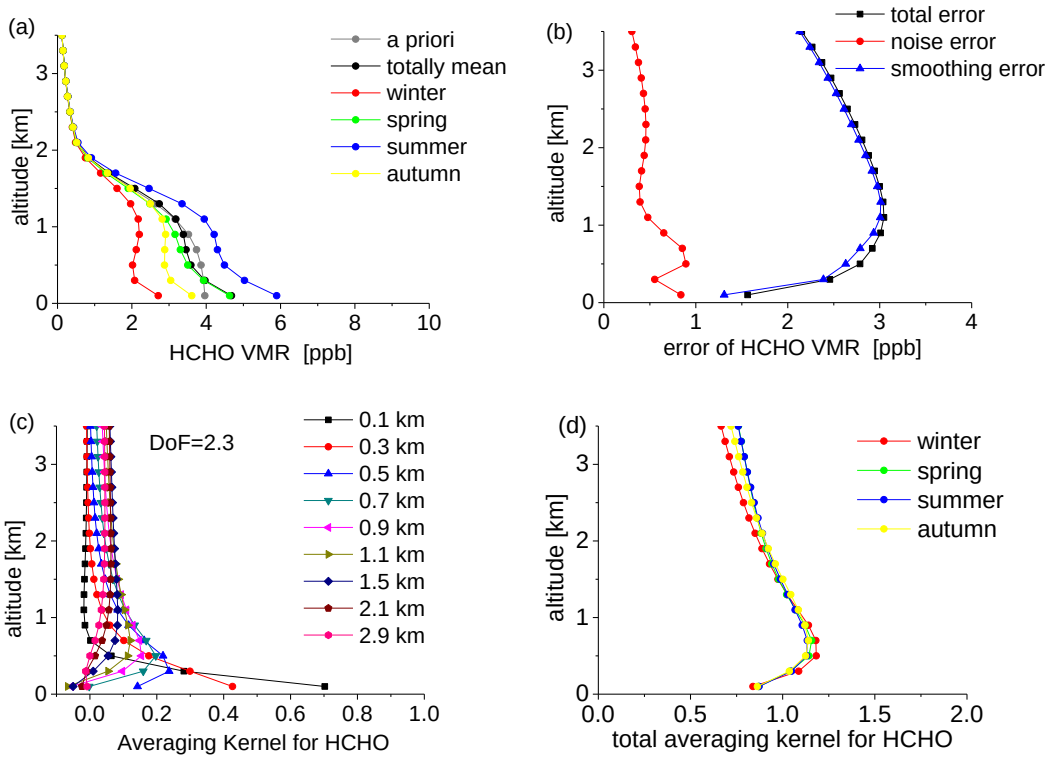

Figure S15: Same as Fig. S12, but for the HCHO retrieval.

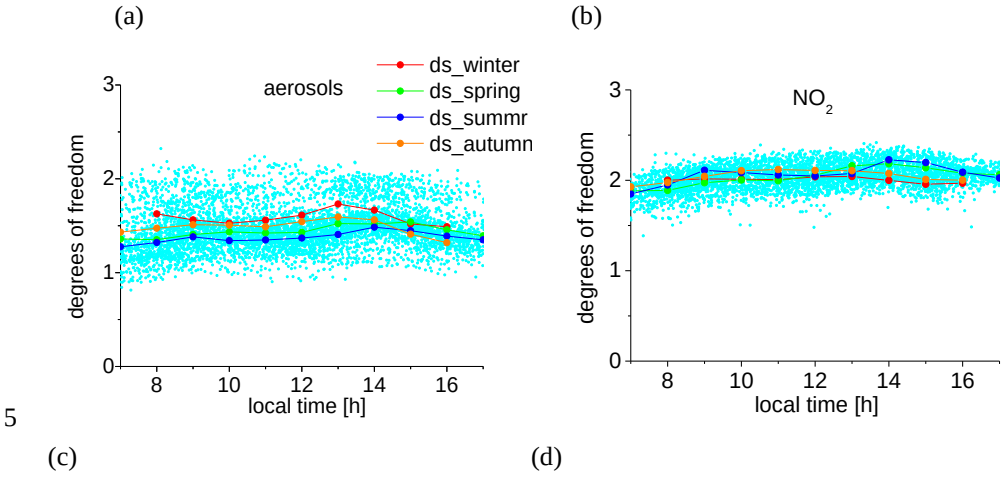

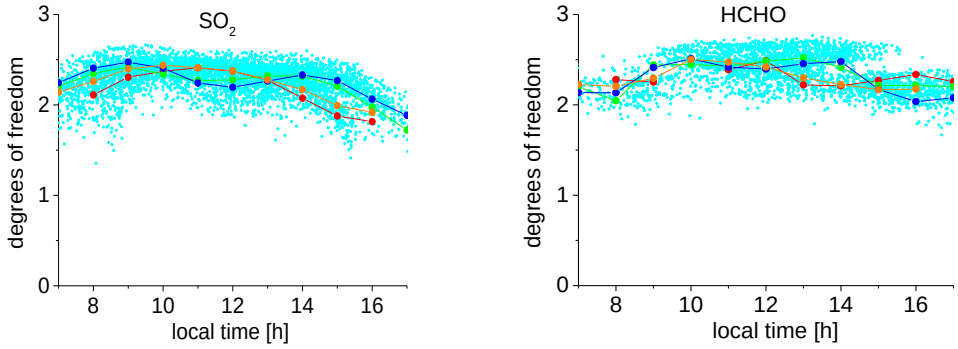

Figure S16: Seasonally averaged diurnal variation of the degree of freedom (ds) of the inversions for aerosols (a), NO_2 (b), SO_2 (c) and HCHO (d). For all four species, the ds in the morning and afternoon is smaller than around noon mainly due to lower scattering probability in the boundary layer.

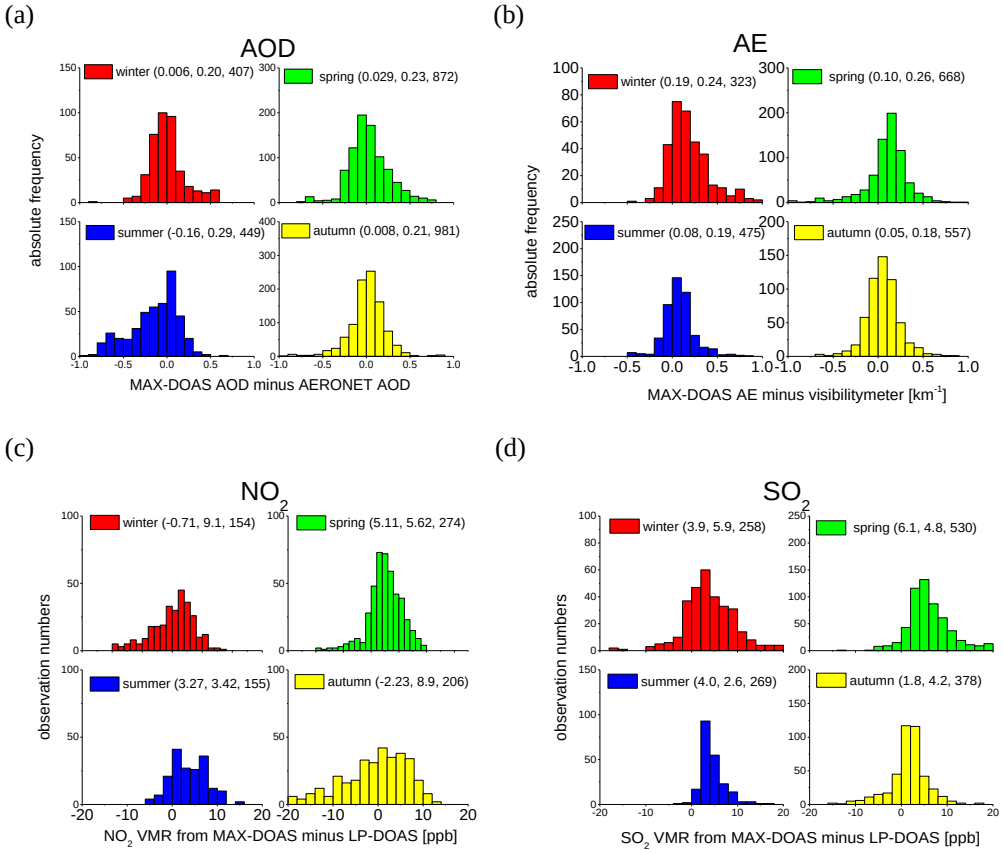

Figure S17: Histograms of the differences between MAX-DOAS results and independent techniques for different seasons for measurements under clear sky conditions with low aerosols. (a) difference of the MAX-DOAS AOD compared with the Taihu AERONET level 1.5 data, (b) difference of the MAX-DOAS AE compared with the results from the visibility meter; (c, d) VMRs of NO_2 and SO_2 derived from MAX-DOAS compared with the results of the nearby long path DOAS instrument. The mean differences, standard deviations and total numbers of observations are given in brackets for each season.

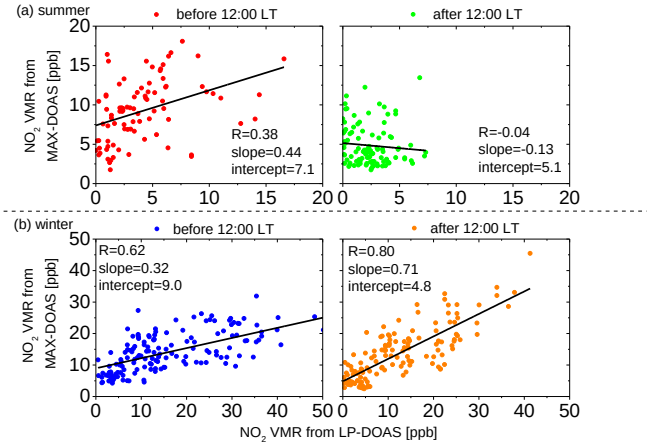

Figure S18: Scatter plots of the near-surface NO_2 VMR derived from MAX-DOAS versus those from LP-DOAS in summer (a) and winter (b) for clear sky conditions with low aerosols. The left and right subfigures show results for morning (before 12:00 local time (LT)) and afternoon (after 12:00 LT), respectively. Results of the linear regression are shown in the individual subfigures.

(a)

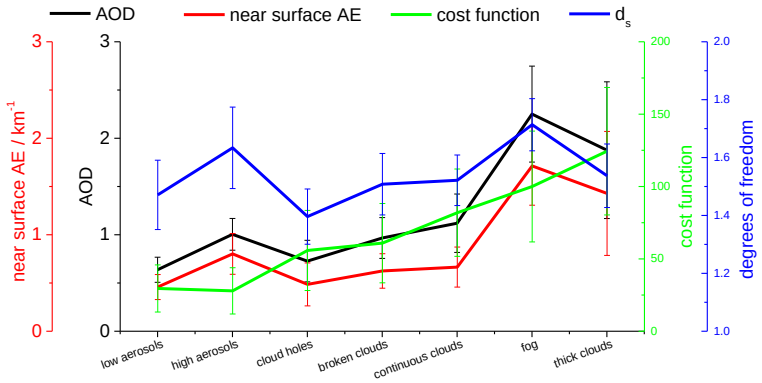

(b)

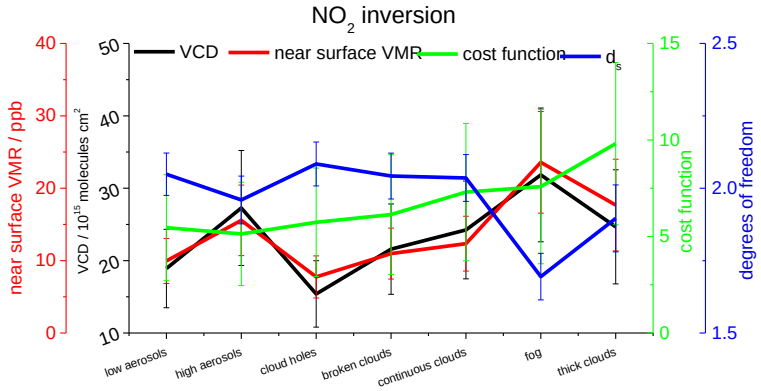

(c)

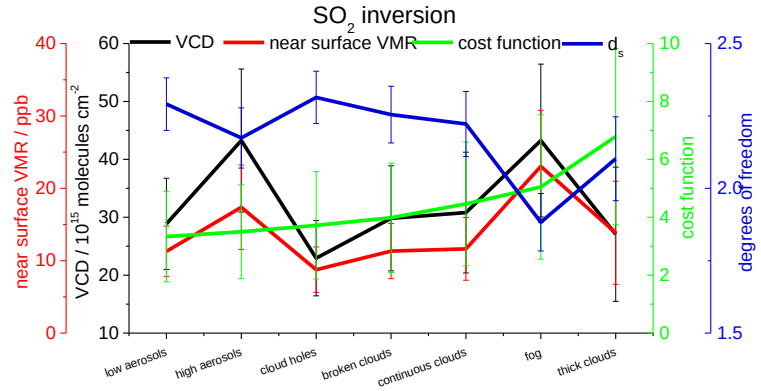

(d)

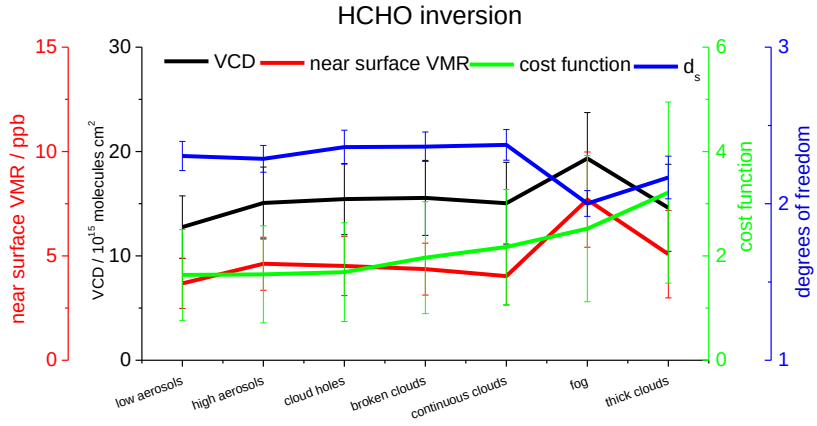

Figure S19: Mean results of all MAX-DOAS retrievals under different sky conditions. Besides the AOD and AE (a) and the trace gas mixing ratios and VCDs (b to d), also the cost functions and degrees of freedom are shown. The cost functions of all species are higher under cloudy conditions compared to clear sky conditions. The effect of clouds is stronger for aerosols compared to TGs. This is consistent with the larger discrepancy between modelled dSCDs and the measured dSCDs shown in Fig. 13 of the main

manuscript. The reason is that clouds are not included in the forward model. The DoF of the inversions strongly depend on the cloud and aerosol load. A large aerosol load leads to an increase of the DoF of the aerosol inversion, but to a decrease of the DoF for the TG inversions. The column densities and near surface TG mixing ratios and AE are found to be quite different for the different sky conditions, probably due to cloud effects on the inversions and the different atmospheric chemistry conditions (photolysis) and dynamics for different cloud conditions.

(a)

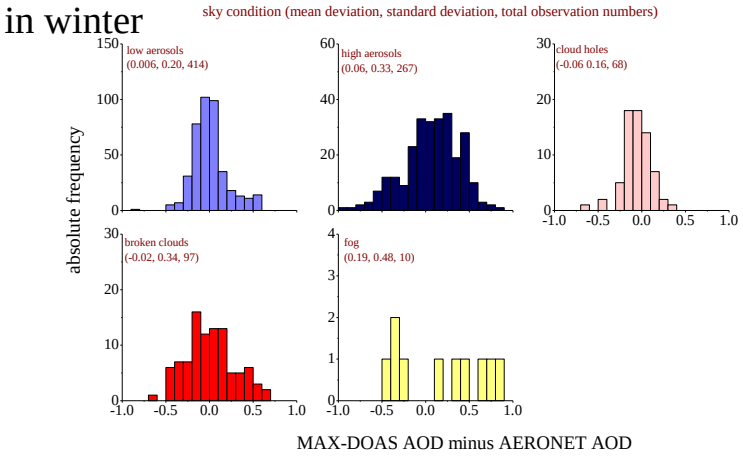

(b)

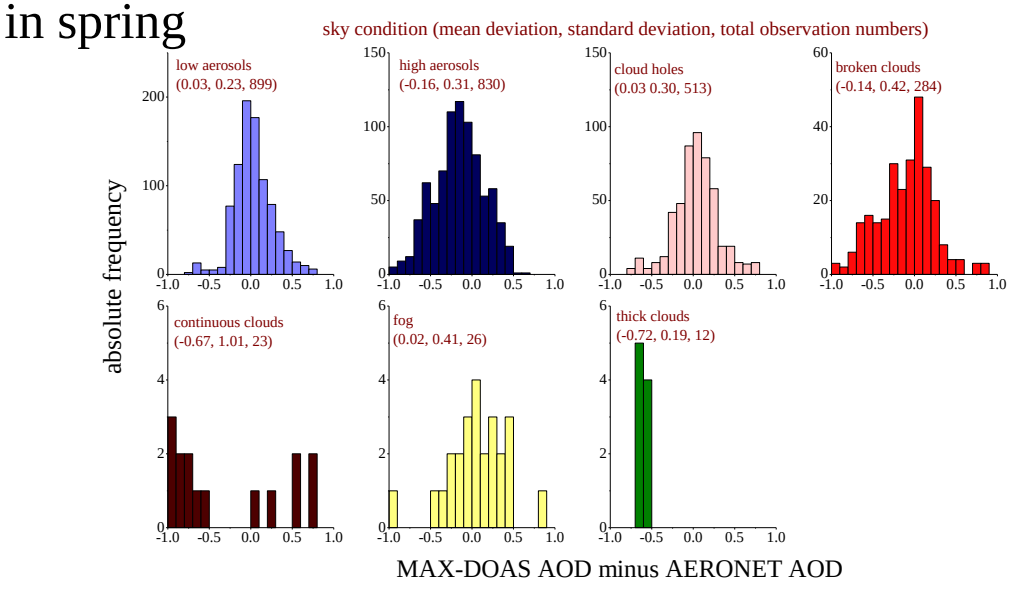

(c)

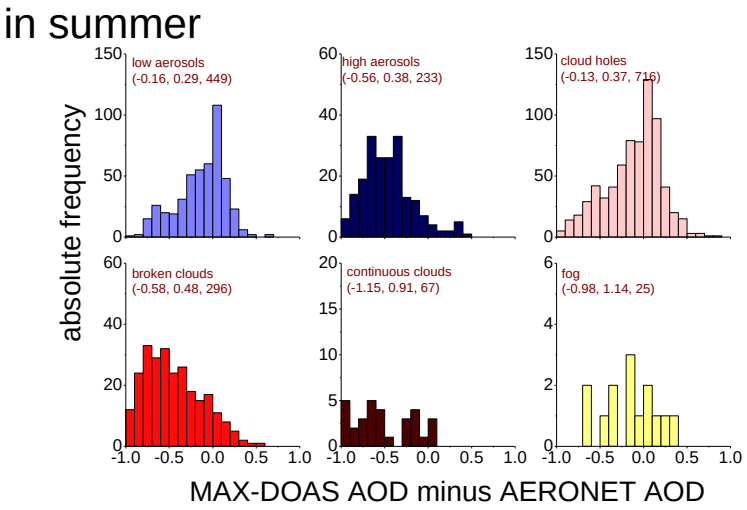
in summer
low aerosols
(-0.16, 0.29, 449)
high aerosols
(-0.56, 0.38, 233)
cloud holes
(-0.13, 0.37, 716)
broken clouds
(-0.58, 0.48, 296)
continuous clouds
(-1.15, 0.91, 67)
fog
(-0.98, 1.14, 25)
absolute frequency
MAX-DOAS AOD minus AERONET AOD

(d)

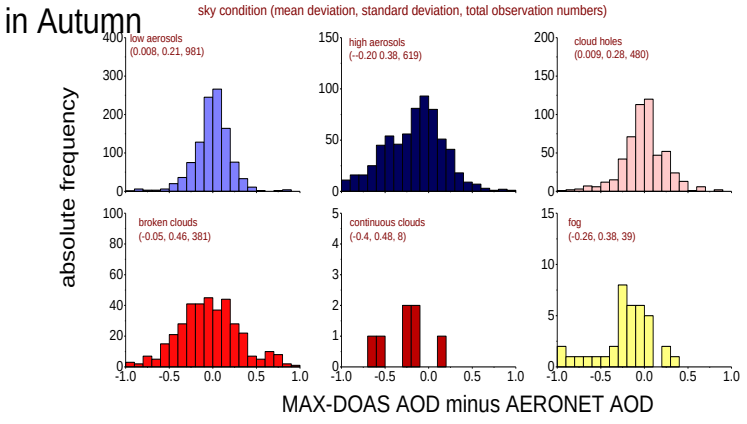
in Autumn
sky condition (mean deviation, standard deviation, total observation numbers)
low aerosols
(0.008, 0.21, 981)
high aerosols
(-0.20 0.38, 619)
cloud holes
(0.009, 0.28, 480)
broken clouds
(-0.05, 0.46, 381)
continuous clouds
(-0.4, 0.48, 8)
fog
(-0.26, 0.38, 39)
absolute frequency
MAX-DOAS AOD minus AERONET AOD

(e) (f)

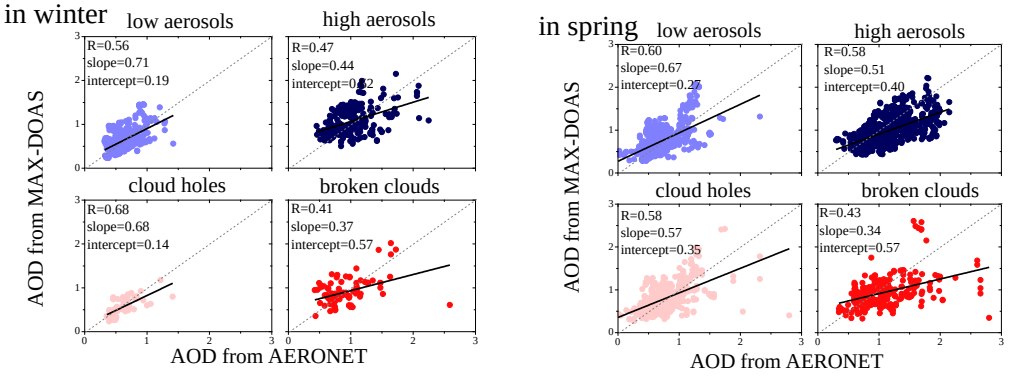
in winter
low aerosols
high aerosols
R=0.56
slope=0.71
intercept=0.19
R=0.47
slope=0.44
cloud holes
broken clouds
R=0.68
slope=0.68
intercept=0.14
R=0.41
slope=0.37
intercept=0.57
AOD from MAX-DOAS
AOD from AERONET
in spring
low aerosols
high aerosols
R=0.60
slope=0.67
intercept=0.27
R=0.58
slope=0.51
intercept=0.40
cloud holes
broken clouds
R=0.58
slope=0.57
intercept=0.35
R=0.43
slope=0.34
intercept=0.57
AOD from MAX-DOAS
AOD from AERONET

5

(g)

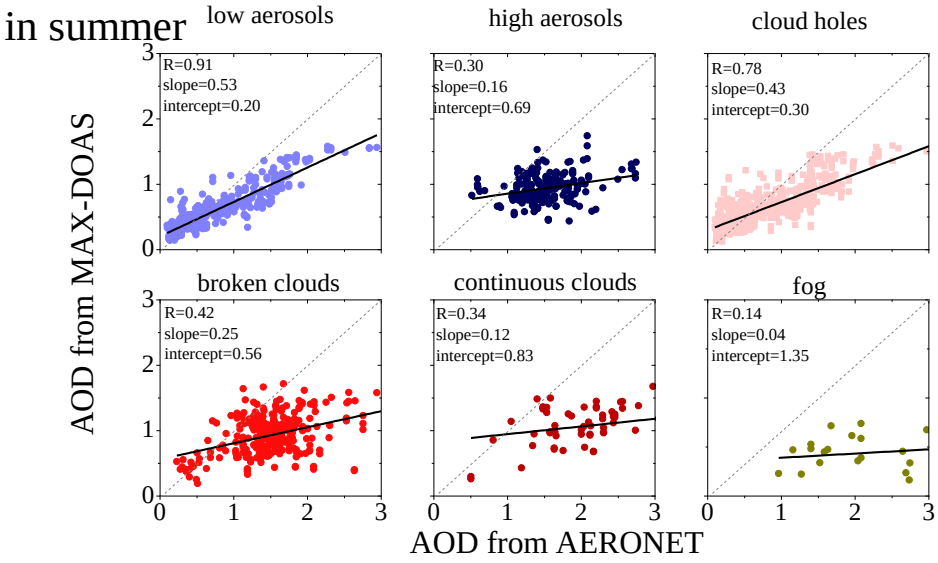

Figure S20: Histograms of the differences of the AOD between MAX-DOAS and the Taihu AERONET observations (level 1.5) under different sky conditions (as identified by the MAX-DOAS observations) in winter (a), spring (b) and summer (c) and autumn (d) for measurements from 2011 to 2013. The mean differences and standard deviations between the two techniques are shown in each subfigure; the AODs from MAX-DOAS are plotted against those from AERONET for different sky conditions; the linear regressions plots are shown in the individual subfigures for winter (e), spring (f) and summer (g). Note that the corresponding scatter plot for autumn is shown in Fig. 16 of the main manuscript.

(a)

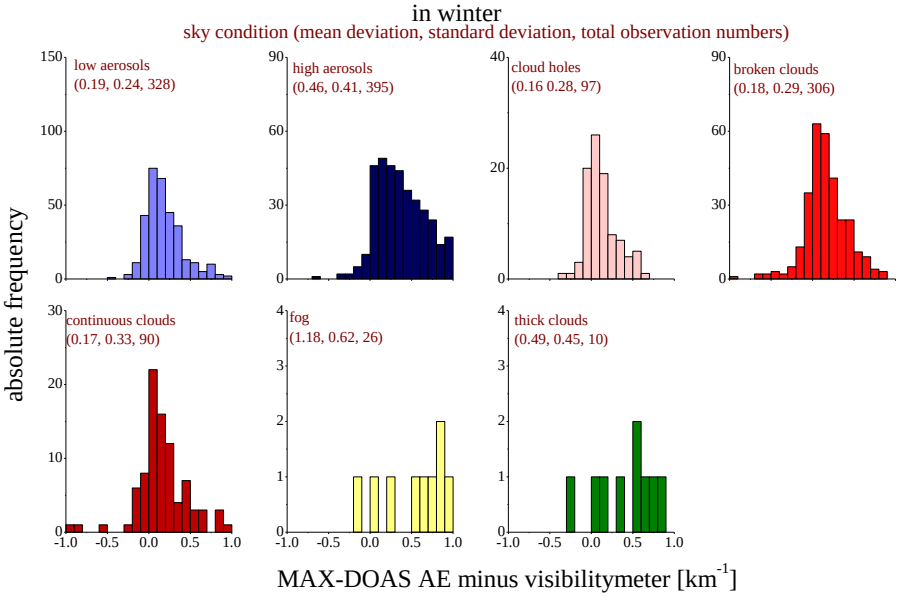

(b)

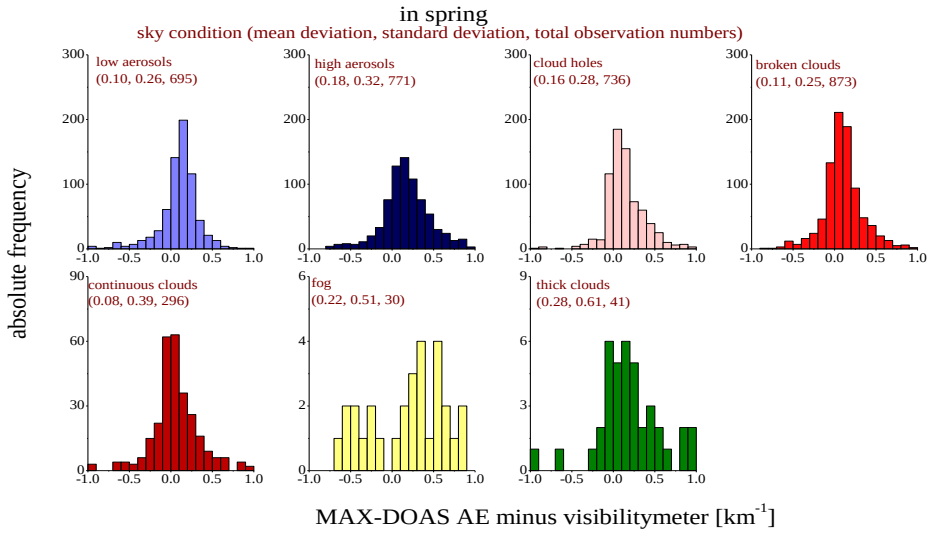
in spring
sky condition (mean deviation, standard deviation, total observation numbers)
low aerosols
(0.10, 0.26, 695)
high aerosols
(0.18, 0.32, 771)
cloud holes
(0.16 0.28, 736)
broken clouds
(0.11, 0.25, 873)
continuous clouds
(0.08, 0.39, 296)
fog
(0.22, 0.51, 30)
thick clouds
(0.28, 0.61, 41)
absolute frequency
MAX-DOAS AE minus visibilitymeter [km-1]

(c)

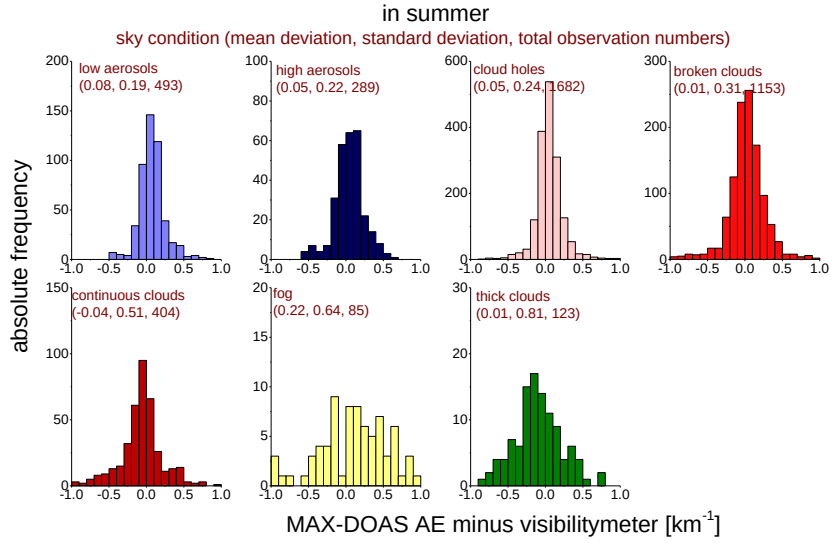
in summer
sky condition (mean deviation, standard deviation, total observation numbers)
low aerosols
(0.08, 0.19, 493)
high aerosols
(0.05, 0.22, 289)
cloud holes
(0.05, 0.24, 1682)
broken clouds
(0.01, 0.31, 1153)
continuous clouds
(-0.04, 0.51, 404)
fog
(0.22, 0.64, 85)
thick clouds
(0.01, 0.81, 123)
absolute frequency
MAX-DOAS AE minus visibilitymeter [km-1]

(d)

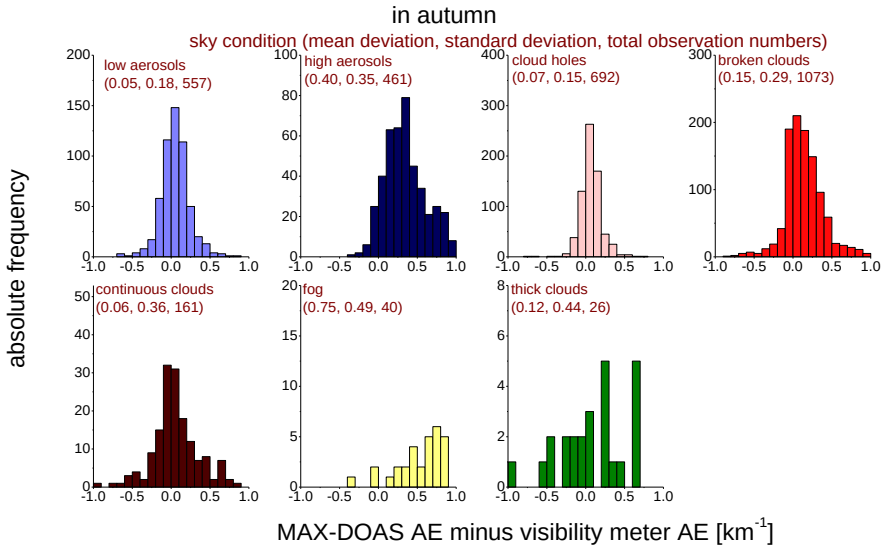
in autumn
sky condition (mean deviation, standard deviation, total observation numbers)
low aerosols
(0.05, 0.18, 557)
high aerosols
(0.40, 0.35, 461)
cloud holes
(0.07, 0.15, 692)
broken clouds
(0.15, 0.29, 1073)
continuous clouds
(0.06, 0.36, 161)
fog
(0.75, 0.49, 40)
thick clouds
(0.12, 0.44, 26)
absolute frequency
MAX-DOAS AE minus visibility meter AE [km-1]

(e)

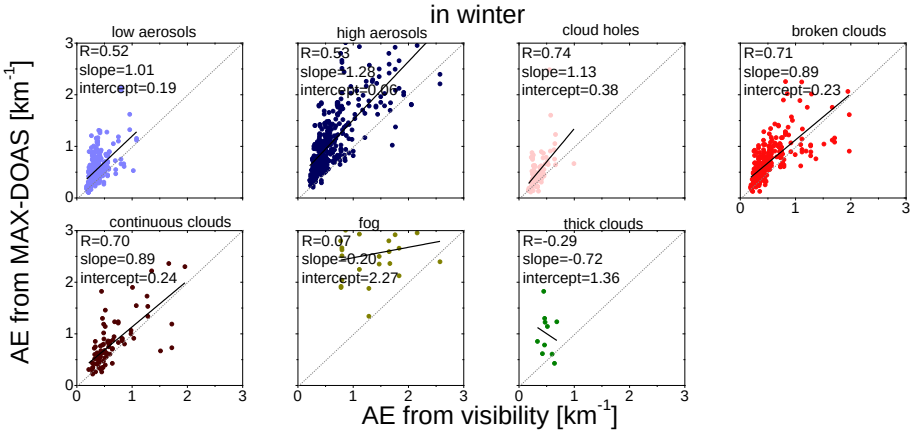
in winter
low aerosols
R=0.52
slope=1.01
intercept=0.19
high aerosols
R=0.53
slope=1.28
intercept=0.06
cloud holes
R=0.74
slope=1.13
intercept=0.38
broken clouds
R=0.71
slope=0.89
intercept=0.23
continuous clouds
R=0.70
slope=0.89
intercept=0.24
fog
R=0.07
slope=0.20
intercept=2.27
thick clouds
R=-0.29
slope=-0.72
intercept=1.36
AE from MAX-DOAS [km-1]
AE from visibility [km-1]

(f)

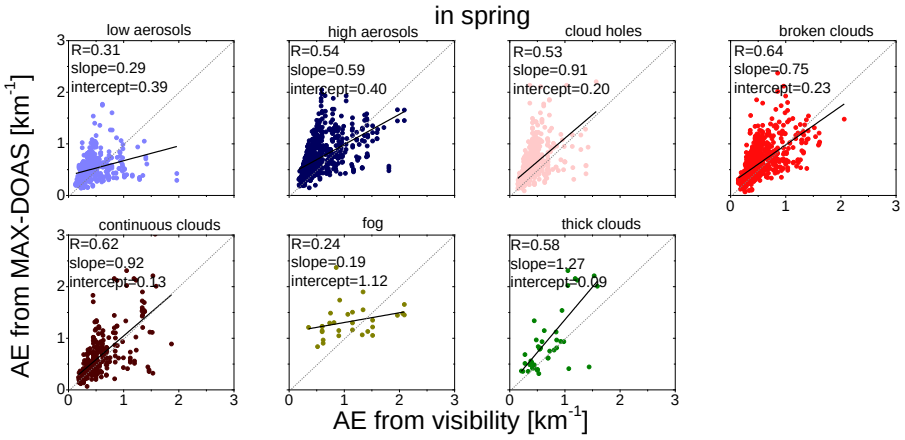

(g)

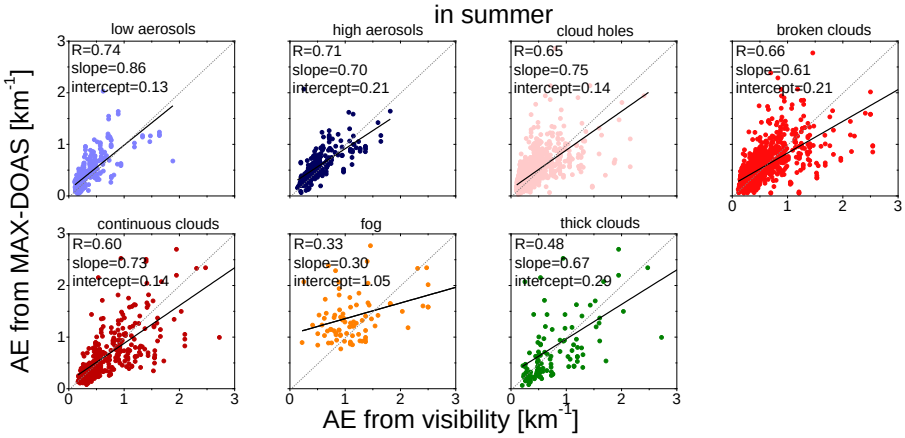

Figure S21: Same as Fig. S20 but for the near-surface aerosol extinction compared with the results from the visibility meter. Note that the corresponding scatter plot for autumn is shown in Fig. 17 of the main manuscript.

(a)

in winter

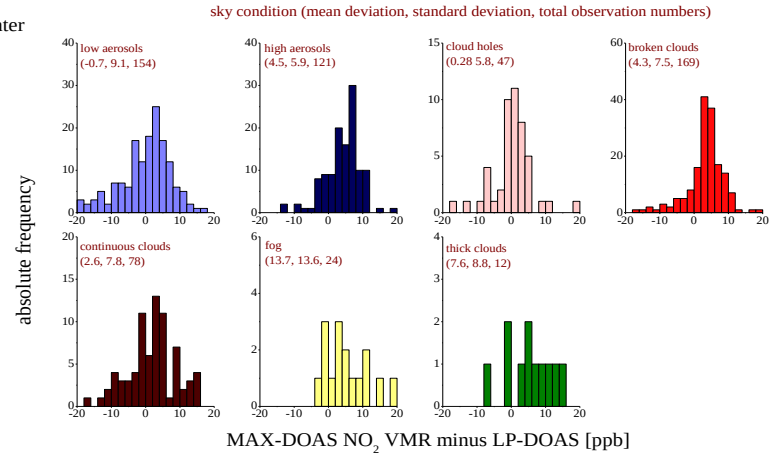

(b)

in spring

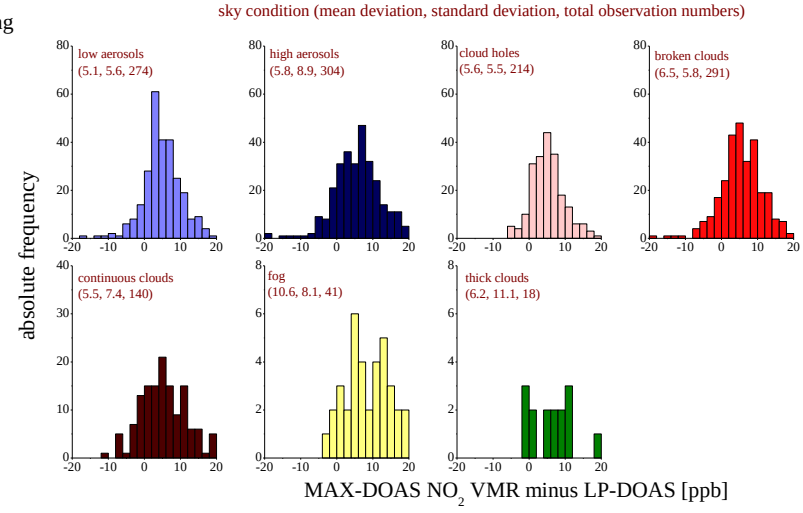

(c)

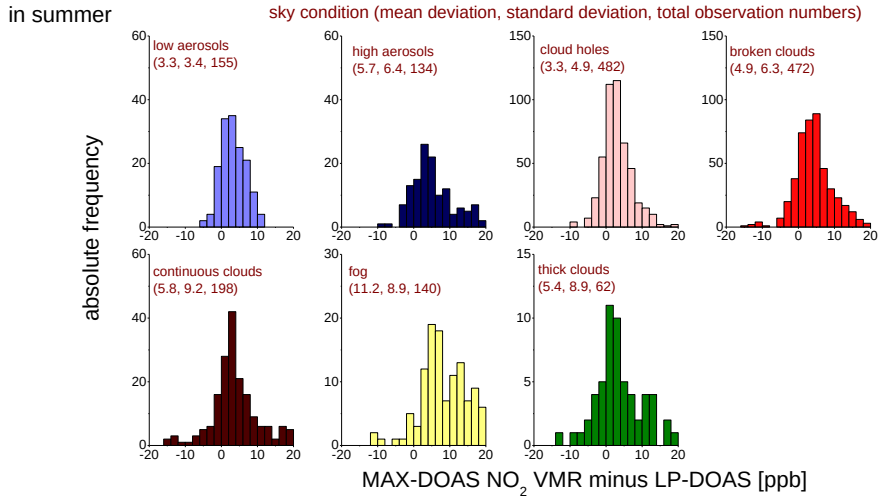
in summer
sky condition (mean deviation, standard deviation, total observation numbers)
low aerosols
(3.3, 3.4, 155)
high aerosols
(5.7, 6.4, 134)
cloud holes
(3.3, 4.9, 482)
broken clouds
(4.9, 6.3, 472)
continuous clouds
(5.8, 9.2, 198)
fog
(11.2, 8.9, 140)
thick clouds
(5.4, 8.9, 62)
absolute frequency
MAX-DOAS NO2 VMR minus LP-DOAS [ppb]

(d)

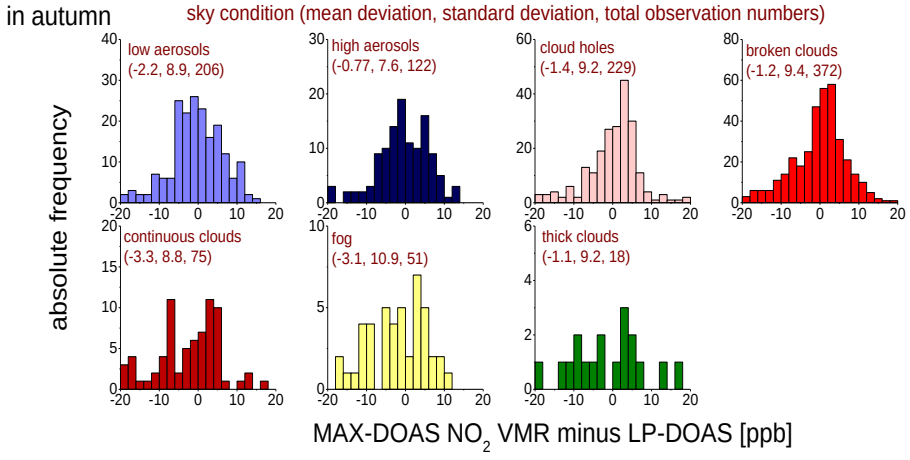
in autumn
sky condition (mean deviation, standard deviation, total observation numbers)
low aerosols
(-2.2, 8.9, 206)
high aerosols
(-0.77, 7.6, 122)
cloud holes
(-1.4, 9.2, 229)
broken clouds
(-1.2, 9.4, 372)
continuous clouds
(-3.3, 8.8, 75)
fog
(-3.1, 10.9, 51)
thick clouds
(-1.1, 9.2, 18)
absolute frequency
MAX-DOAS NO2 VMR minus LP-DOAS [ppb]

(e)

in winter

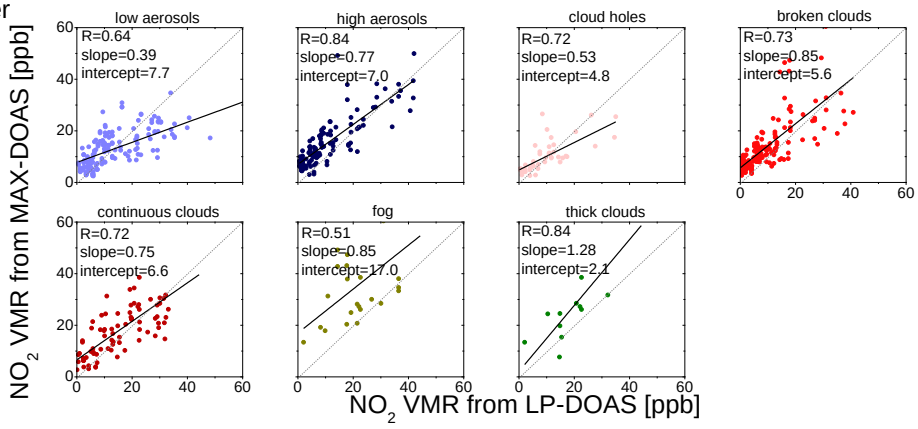

(f)

in spring

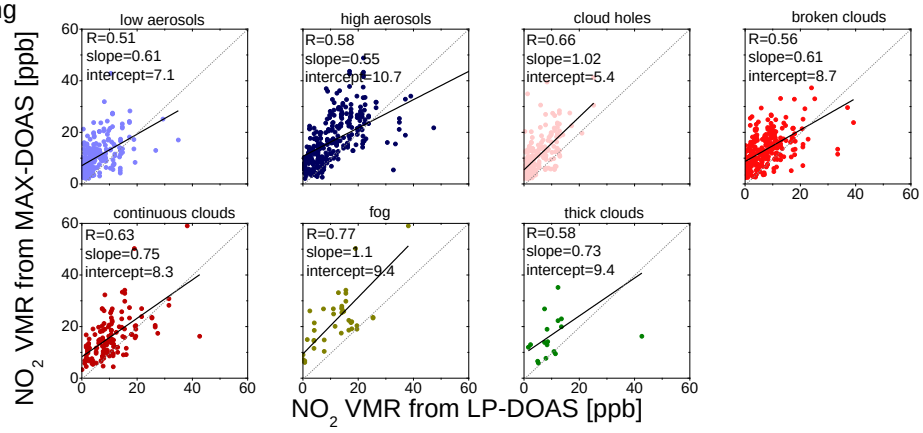

(g)

in summer

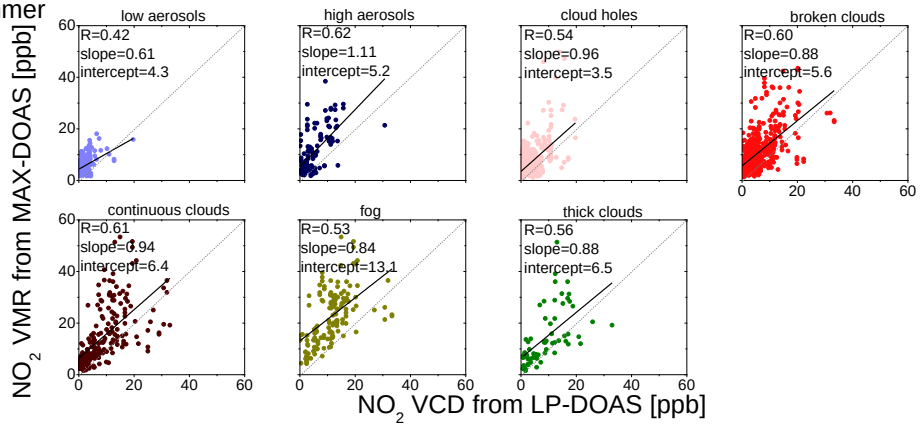

Figure S22: Same as Fig. S20 but for the near-surface NO_2 VMRs compared with the results from LP-DOAS. Note that the corresponding scatter plot for autumn is shown in Fig. 18 of the main manuscript.

(a)

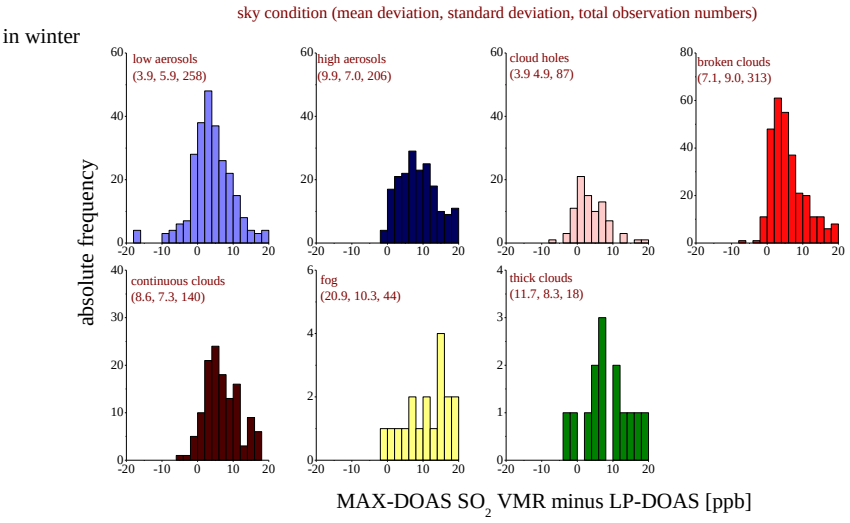

(b)

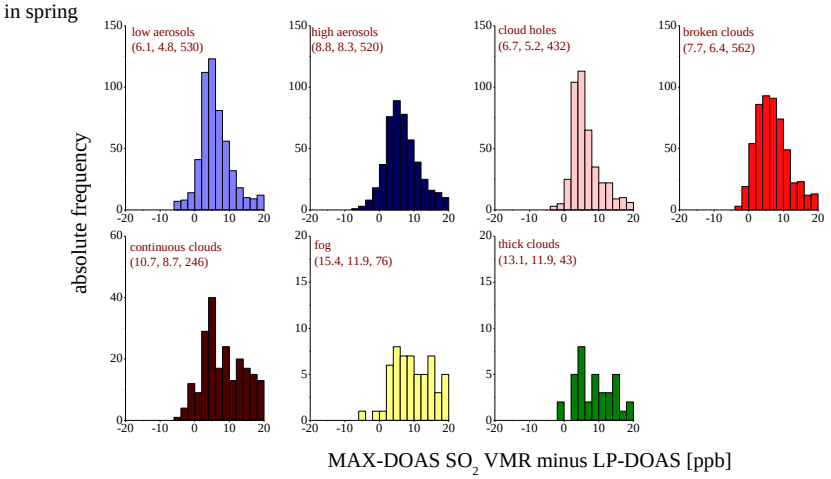

(c)

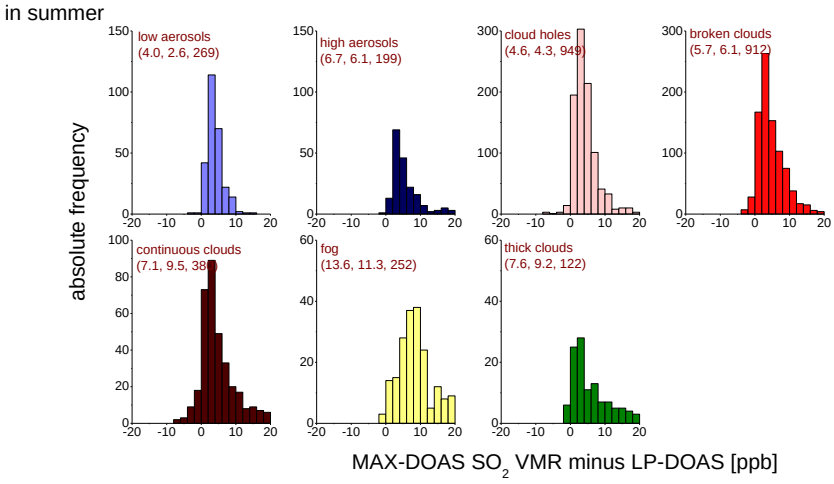
in summer
low aerosols
(4.0, 2.6, 269)
high aerosols
(6.7, 6.1, 199)
cloud holes
(4.6, 4.3, 949)
broken clouds
(5.7, 6.1, 912)
continuous clouds
(7.1, 9.5, 388)
fog
(13.6, 11.3, 252)
thick clouds
(7.6, 9.2, 122)
absolute frequency
MAX-DOAS SO2 VMR minus LP-DOAS [ppb]

(d)

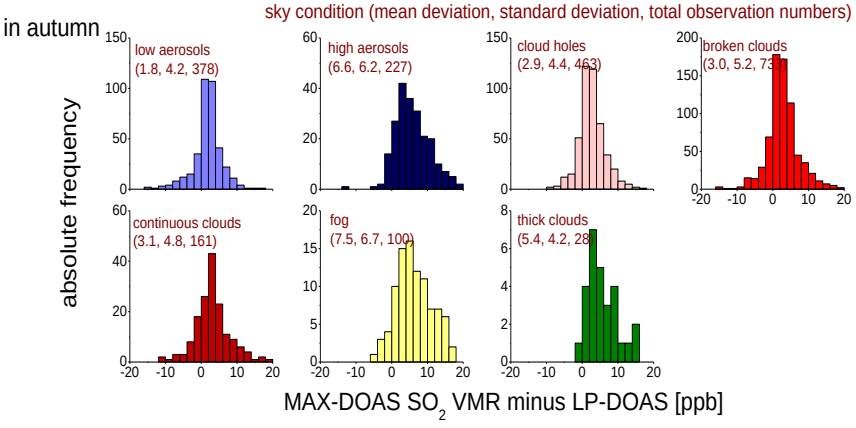
in autumn
sky condition (mean deviation, standard deviation, total observation numbers)
low aerosols
(1.8, 4.2, 378)
high aerosols
(6.6, 6.2, 227)
cloud holes
(2.9, 4.4, 463)
broken clouds
(3.0, 5.2, 73
continuous clouds
(3.1, 4.8, 161)
fog
(7.5, 6.7, 100)
thick clouds
(5.4, 4.2, 28
absolute frequency
MAX-DOAS SO2 VMR minus LP-DOAS [ppb]

(e)

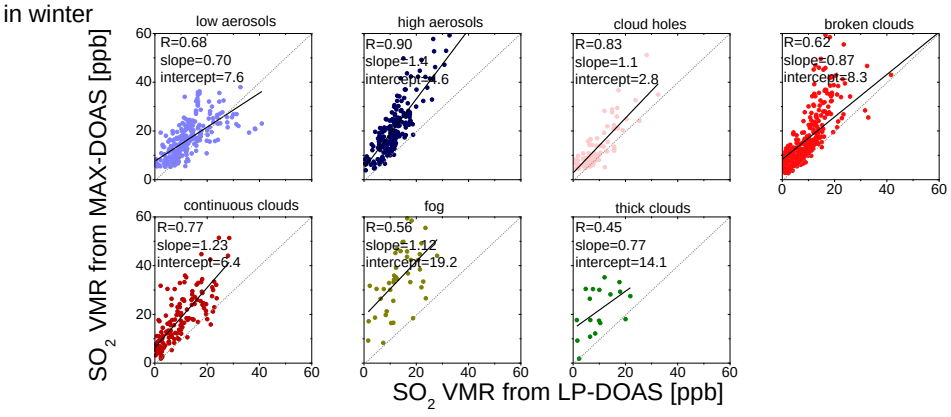
in winter
low aerosols
R=0.68
slope=0.70
intercept=7.6
high aerosols
R=0.90
slope=1.1
intercept=4.6
cloud holes
R=0.83
slope=1.1
intercept=2.8
broken clouds
R=0.62
slope=0.87
intercept=8.3
continuous clouds
R=0.77
slope=1.23
intercept=6.4
fog
R=0.56
slope=1.12
intercept=19.2
thick clouds
R=0.45
slope=0.77
intercept=14.1
SO2 VMR from MAX-DOAS [ppb]
SO2 VMR from LP-DOAS [ppb]

(f)

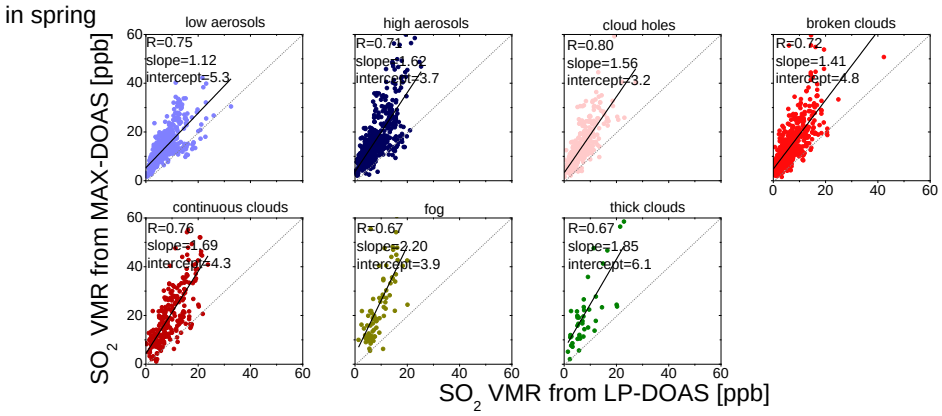

(g)

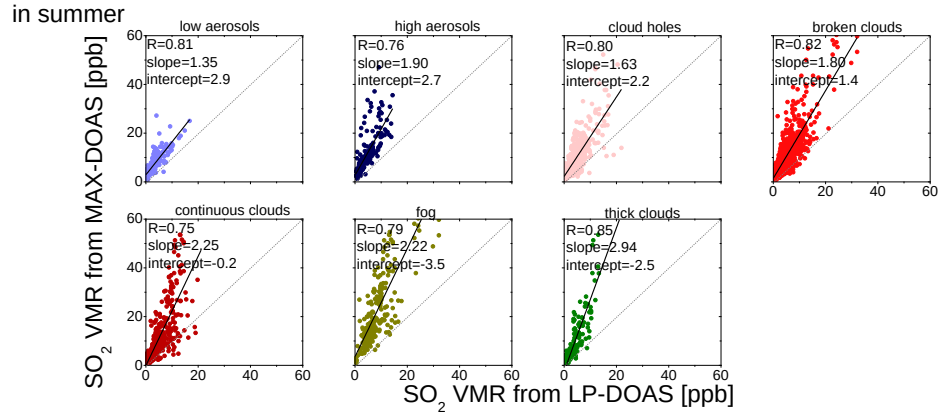

Figure S23: Same as Fig. S20 but for the near-surface SO_2 VMRs compared with the results from LP-DOAS. Note that the corresponding scatter plot for autumn is shown in Fig. 19 of the main manuscript.

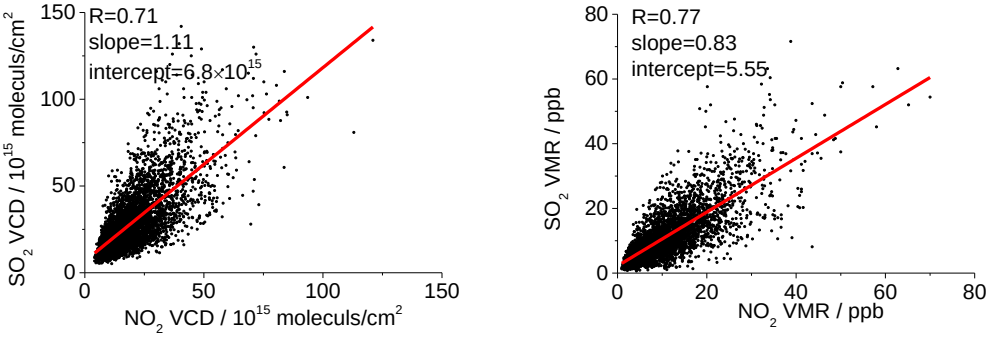

Figure S24: SO_2 VCDs (a) and VMRs near surface (b) plotted against NO_2 VCDs and VMRs, respectively. The linear regressions are shown in each subfigure.

(a)

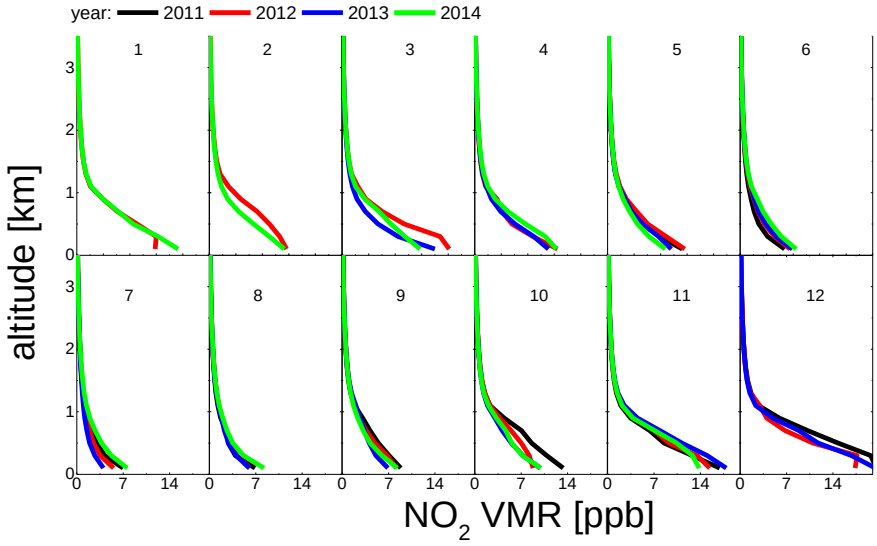
year: 2011 2012 2013 2014
1
2
3
4
5
6
7
8
9
10
11
12
altitude [km]
NO2 VMR [ppb]

(b)

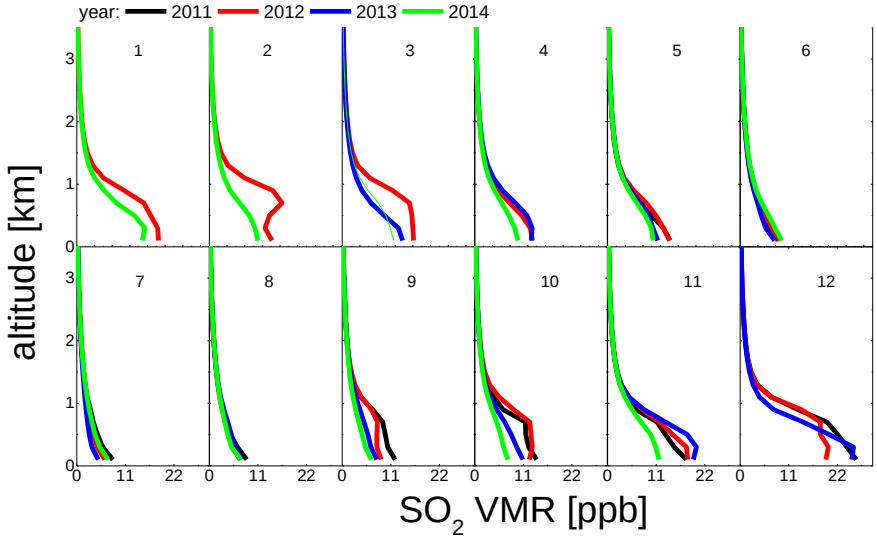
year: 2011 2012 2013 2014
1
2
3
4
5
6
7
8
9
10
11
12
altitude [km]
SO2 VMR [ppb]

(c)

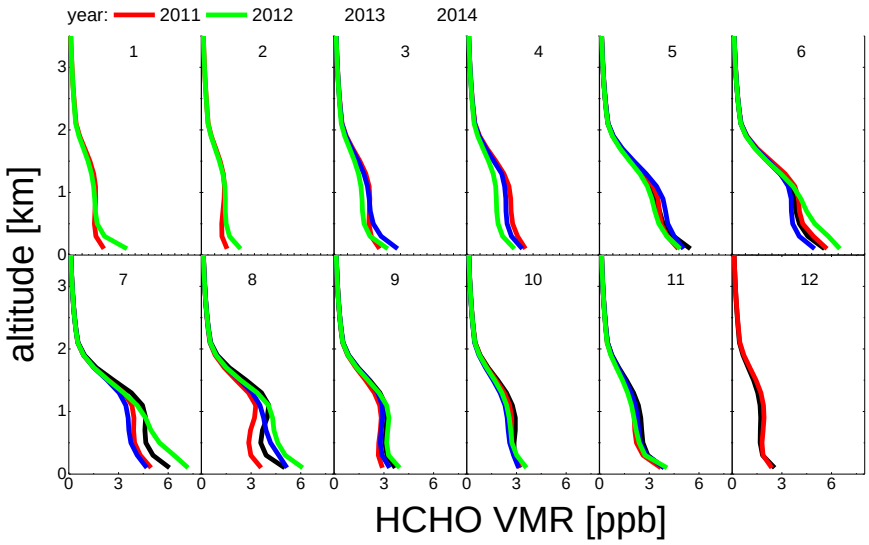

Figure S25: Monthly mean profiles of NO_2 (a), SO_2 (b), HCHO (c) VMRs under clear sky conditions for May 2011 to November 2014.

(a) (b) (c)

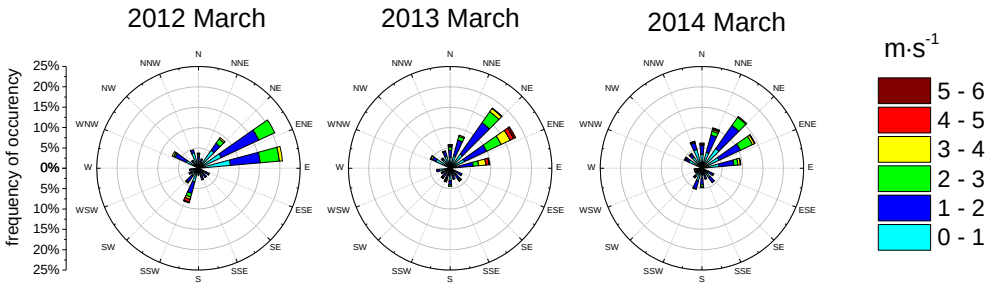

Figure S26: Wind roses for March 2012 (a), 2013 (b) and 2014(c).

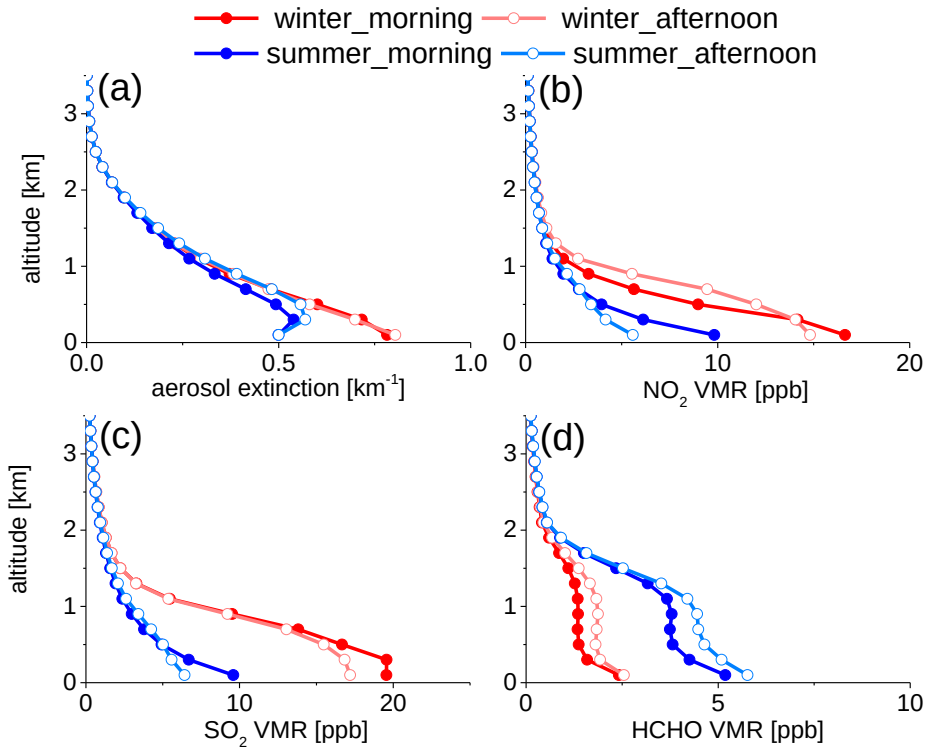

Figure S27: Average profiles of aerosol extinction (a), NO_2 VMR (b), SO_2 VMR (c) and HCHO VMR (d) in the morning and afternoon for winter and summer, respectively.

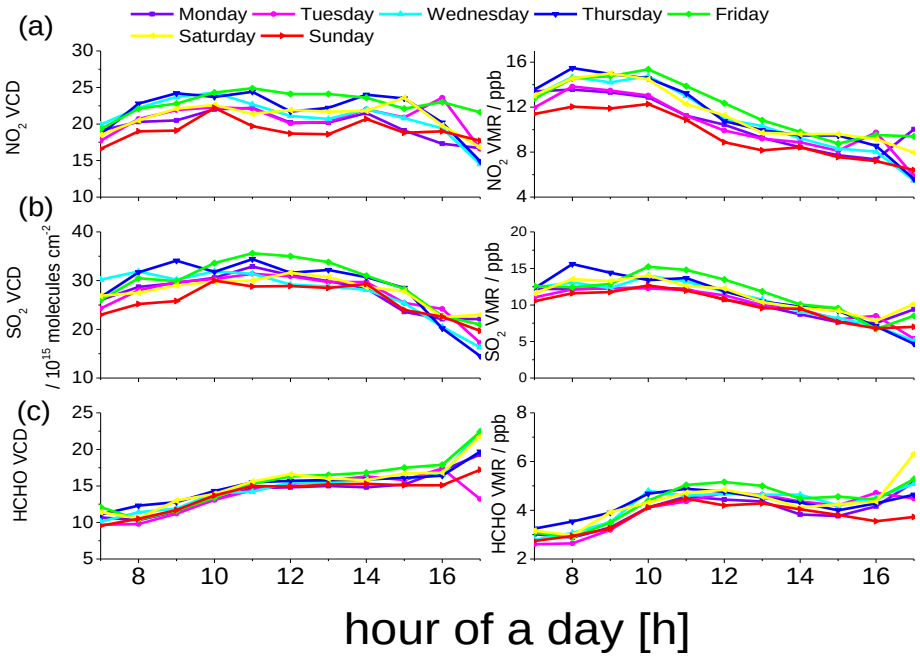

Figure S28: Diurnal variations of VCDs (left) and surface VMR (right) of NO_2 (a), SO_2 (b) and HCHO (c) for different days of the week, averaged over the period of May 2011 to November 2014.

Table S1 Absolute and relative differences of the retrieved VCDs (and AOD) and near-surface VMRs (AEs) of NO_2, SO_2 and HCHO between either using the three test a-priori profiles or the standard a-priori profile (shown in Fig. S6)

species	a-priori profile	Absolute difference		Relative difference	
		VCD (10^{15} molecules cm^{-2}) or AOD	Near-surface VMR (ppb) or AE (km^{-1})	VCD or AOD	Near-surface VMR or AE
aerosols	Priori 1	-0.17	0.05	-24%	10%
	Priori 2	0.11	0.003	15%	0.6%
	Priori 3	-0.16	0.67	22%	136%
NO_2	Priori 1	-1.7	-0.29	-7%	2.2%
	Priori 2	2.4	0.18	10%	1.3%
	Priori 3	2.7	0.09	11%	0.7%
SO_2	Priori 1	-3.1	-0.21	-10%	-2%
	Priori 2	3.9	0.10	12%	1%
	Priori 3	2.3	-0.17	7%	-1%
HCHO	Priori 1	-0.22	-0.027	-1%	-0.5%
	Priori 2	0.85	0.049	5%	1%
	Priori 3	-1.1	-0.025	-7%	-0.5%

References

Bussemer, M.: Der Ring-Effekt: Ursachen und Einfluß auf die Messung stratosparischer Spurenstoffe, Diploma thesis, University of Heidelberg, 1993.

Chance, K. V. and Spurr, R. J. D.: Ring effect studies: Rayleigh scattering, including molecular parameters for rotational Raman scattering, and the Fraunhofer spectrum, Appl. Optics, 36, 5224–5230, 1997.

Coburn, S., Dix, B., Sinreich, R., and Volkamer, R.: The CU ground MAX-DOAS instrument: characterization of RMS noise limitations and first measurements near Pensacola, FL of BrO, IO, and CHOCHO, Atmos. Meas. Tech., 4, 2421-2439, doi:10.5194/amt-4-2421-2011, 2011.

Frieß, U., Monks, P. S., Remedios, J. J., Rozanov A., Sinreich R., Wagner T., and Platt, U.: MAX-DOAS O_4 measurements: A new technique to derive information on atmospheric aerosols: 2. Modeling studies, J. Geophys. Res., 111, D14203, 2006, doi:10.1029/2005JD006618.

Grainger J. F. and Ring, J.: Anomalous Fraunhofer line profiles, Nature, 193, 762, 1962.

Hendrick, F., Müller, J.-F., Clémer, K., Wang, P., De Mazière, M., Fayt, C., Gielen, C., Hermans, C., Ma, J. Z., Pinardi, G., Stavrakou, T., Vlemmix, T., and Van Roozendael, M.: Four years of ground-based MAX-DOAS observations of HONO and NO2 in the Beijing area, Atmos. Chem. Phys., 14, 765-781, doi:10.5194/acp-14-765-2014, 2014.

Holla, R., Schmitt, S., Friess, U., Pöhler, D., Zingler, J., Corsmeier, U., and Platt, U.: Vertical distribution of BrO in the boundary layer at the Dead Sea. Environmental Chemistry, 2015.

Hönninger, G., Friedeburg, C. von and Plat, U., Multi axis differential optical absorption spectroscopy (MAX-DOAS), Atmos. Chem. Phys., 4, 231–254, 2004

Junkermann, W.: On the distribution of formaldehyde in the western Po-Valley, Italy, during FORMAT 2002/2003, Atmos. Chem. Phys., 9, 9187–9196, doi:10.5194/acp-9-9187-2009, 2009.

Kraus, S.: DOASIS, A Framework Design for DOAS, PhD-thesis, University of lMannheim,http://hci.iwr.uni-heidelberg.de/publications/dip/2006/Kraus_PhD2006.pdf, 2006.

Pinardi, G., Van Roozendael, M., Abuhassan, N., Adams, C., Cede, A., Clémer, K., Fayt, C., Frieß, U., Gil, M., Herman, J., Hermans, C., Hendrick, F., Irie, H., Merlaud, A., Navarro Comas, M., Peters, E., Piters, A. J. M., Puentedura, O., Richter, A., Schönhardt, A., Shaiganfar, R., Spinei, E., Strong, K., Takashima, H., Vrekoussis, M., Wagner, T., Wittrock, F., and Yilmaz, S.: MAX-DOAS formaldehyde slant column measurements during CINDI: intercomparison and analysis improvement, Atmos. Meas. Tech., 6, 167-185, doi:10.5194/amt-6-167-2013, 2013.

Rodgers, C. D.: Inverse methods for atmospheric sounding, theory and practice, Series on Atmospheric, Oceanic and Planetary Physics, World Scientific, 2000.

Shefov, N. N.: Spectroscopic, photoelectric, and radar investigations of the aurora and the nightglow, Izd. Akad. Nauk., 1, 1959.

Solomon, S., Schmeltekopf, A. L. and Sanders, R. W.: On the interpretation of zenith sky absorption measurements, J. Geophys. Res., 92, 8311–8319, 1987.

Wagner, T., B. Dix, C. von Friedeburg, Frieß, U., Sanghavi, S., Sinreich, R. and Platt, U.: MAX-DOAS O_4 measurements: A new technique to derive information on atmospheric aerosols—Principles and information content, J. Geophys. Res., 109, D22205, 2004.

Wagner, T., Beirle, S., and Deutschmann, T.: Three-dimensional simulation of the Ring effect in observations of scattered sun light using Monte Carlo radiative transfer models, Atmos. Meas. Tech., 2, 113-124, 2009.

Wagner, T., Beirle, S., Brauers, T., Deutschmann, T., Frieß, U., Hak, C., Halla, J. D., Heue, K. P., Junkermann, W., Li, X., Platt, U. and Pundt-Gruber, I.: Inversion of tropospheric profiles of aerosol extinction and HCHO and NO_2 mixing ratios from MAX-DOAS observations in Milano during the summer of 2003 and comparison with independent data sets, Atmos. Meas. Tech. Discuss, 4, 3891–3964, 2011.

Wang, T., Hendrick, F., Wang, P., Tang, G., Clémer, K., Yu, H., Fayt, C., Hermans, C., Gielen, C., Müller, J.-F., Pinardi, G., Theys, N., Brenot, H., and Van Roozendael, M.: Evaluation of tropospheric SO_2 retrieved from MAX-DOAS measurements in Xianghe, China, Atmos. Chem. Phys., 14, 11149-11164, doi:10.5194/acp-14-11149-2014, 2014

Yilmaz, S.: Retrieval of Atmospheric Aerosol and Trace Gas Vertical Profiles using Multi-Axis Differential Optical Absorption Spectroscopy, Dissertation submitted to the Combined Faculties for the Natural Sciences and for Mathematics of the Ruperto-Carola University of Heidelberg, Germany for the degree of Doctor of Natural Sciences, 2012.